

# Autoencoders in Function Space

**Justin Bunker**

*Department of Engineering  
University of Cambridge  
Cambridge, CB2 1TN, United Kingdom*

JB2200@CANTAB.AC.UK

**Mark Girolami**

*Department of Engineering, University of Cambridge  
and Alan Turing Institute  
Cambridge, CB2 1TN, United Kingdom*

MGIROLAMI@TURING.AC.UK

**Hefin Lambley**

*Mathematics Institute  
University of Warwick  
Coventry, CV4 7AL, United Kingdom*

HEFIN.LAMBLEY@WARWICK.AC.UK

**Andrew M. Stuart**

*Computing + Mathematical Sciences  
California Institute of Technology  
Pasadena, CA 91125, United States of America*

ASTUART@CALTECH.EDU

**T. J. Sullivan**

*Mathematics Institute & School of Engineering  
University of Warwick  
Coventry, CV4 7AL, United Kingdom*

T.J.SULLIVAN@WARWICK.AC.UK

## Abstract

Autoencoders have found widespread application, in both their original deterministic form and in their variational formulation (VAEs). In scientific applications it is often of interest to consider data that are comprised of functions; the same perspective is useful in image processing. In practice, discretisation (of differential equations arising in the sciences) or pixellation (of images) renders problems finite dimensional, but conceiving first of algorithms that operate on functions, and only then discretising or pixellating, leads to better algorithms that smoothly operate between different levels of discretisation or pixellation. In this paper function-space versions of the autoencoder (FAE) and variational autoencoder (FVAE) are introduced, analysed, and deployed. Well-definedness of the objective function governing VAEs is a subtle issue, even in finite dimension, and more so on function space. The FVAE objective is well defined whenever the data distribution is compatible with the chosen generative model; this happens, for example, when the data arise from a stochastic differential equation. The FAE objective is valid much more broadly, and can be straightforwardly applied to data governed by differential equations. Pairing these objectives with neural operator architectures, which can thus be evaluated on any mesh, enables new applications of autoencoders to inpainting, superresolution, and generative modelling of scientific data.

**Keywords:** Variational inference on function space; operator learning; variational autoencoders; regularised autoencoders; scientific machine learning.

## 1 Introduction

Functional data, or data that can be thought of as a high-resolution approximation of functional data, is ubiquitous in data science (Ramsay and Silverman, 2002). Recent years have seen increasing interest in machine learning in this setting, with the promise of architectures that can be discretised, trained, and evaluated across resolutions. A variety of methods now exist for the supervised learning of operators mapping between function spaces, starting with the early paper of Chen and Chen (1993), followed by DeepONet (Lu et al., 2021) and PCA-Net (Bhattacharya et al., 2021) and leading to Fourier neural operators (FNOs; Li et al., 2021) and variants (Kovachki et al., 2023). This function-space perspective has proven successful in applications such as surrogate modelling for expensive numerical simulators of dynamical systems (Azizzadenesheli et al., 2024).

Practical algorithms for functional data must necessarily operate on finite-dimensional representations of the underlying infinite-dimensional objects, ideally by identifying salient features independent of the data resolution. Some models such as PCA-Net and DeepONet make this dimension reduction explicit by representing outputs as a linear combination of basis functions learned from data, while others do this implicitly, as in, for example, the deep layered structure of FNOs involving repeated application of the discrete Fourier transform followed by pointwise activation.

Linear dimension-reduction methods such as principal component analysis are readily adapted to function space, and indeed this is the foundation of PCA-Net; but there are many types of data, such as solutions to advection-dominated partial differential equations (PDEs), for which linear approximations are provably inefficient—a phenomenon known as the Kolmogorov barrier (Peherstorfer, 2022). This suggests the need for nonlinear dimension-reduction techniques on function space. Motivated by this we propose an extension of variational autoencoders (VAEs; Kingma and Welling, 2014) to functional data using operator learning; we refer to the resulting model as the **functional variational autoencoder (FVAE)**. As a probabilistic latent-variable model, the FVAE allows for both dimension reduction and principled generative modelling.

To ensure that the variational objective is defined in function space, we average the usual VAE loss over the data distribution, revealing the need for a **finite-information condition** forbidding the FVAE generative model from being misspecified relative to the data. This condition has received little attention hitherto but is in fact present in finite-dimensional settings; its failure leads to foundational issues in the probabilistic interpretation of FVAE and practical training issues in the infinite-resolution and infinite-data limits. Prior work on adapting VAEs to function space, e.g., the variational autoencoding neural operator (VANO; Seidman et al., 2023), have already shown promising empirical results, but the barriers we discover render the meaning of the variational objective unclear without suitable conditions on the data. Our applications of FVAE rest on establishing decoder noise with the correct level of regularity so that the objective is defined, and we show that this is possible for numerous problems in the physical sciences (Stuart, 2010; Hairer et al., 2011).

However, there are many problems arising in the sciences, and in generative models for partial differential equations in particular, for which application of VAEs on function space fails because the model is typically misspecified relative to the data distribution. To overcome this we propose a deterministic regularised autoencoder that can be applied in

very general settings, which we call the **functional autoencoder (FAE)**. We complement the FVAE and FAE objectives with encoder and decoder architectures based on neural operators that can be discretised on arbitrary, and possibly distinct, meshes. The ability to discretise both encoder and decoder on any mesh extends prior work and is highly empowering, enabling a variety of novel applications of the autoencoder methodology to scientific data, including inpainting and superresolution.

**Contributions.** We make the following contributions to the development and application of autoencoders in the setting of functional data:

- (C1) we propose FVAE, an extension of VAEs to function space, finding that the training objective makes sense only under a finite-information condition ensuring compatibility between the data distribution and the generative model associated with FVAE;
- (C2) we complement our training objective with architectures that permit discretisation on any mesh—even irregular, non-grid meshes—and propose a self-supervised training scheme exploiting the ability to evaluate the encoder and decoder on distinct meshes;
- (C3) we show numerically and analytically that a failure of the finite-information condition in (C1) can lead to a divergence of the training loss in the infinite-resolution or infinite-data limits, or a breakdown of the probabilistic foundations of FVAE;
- (C4) we propose FAE, an extension of regularised autoencoders to function space, and show that this objective is defined in many situations where FVAE fails;
- (C5) we validate FAE and FVAE numerically on examples from across science and engineering, including data arising from stochastic differential equations (SDEs) and from PDEs, and in so doing we demonstrate the value of having both an encoder and decoder that can be discretised on any mesh by using our mesh-invariant autoencoders for inpainting, superresolution, and generative modelling.

**Outline.** In Section 2, we extend VAEs to function space under the condition described in (C1) forbidding misspecification of the generative model. This condition is significant in infinite dimensions, but is satisfied, for example, when the data are realisations of an SDE. We then state the mesh-invariant architectures described in (C2) and validate our approach, FVAE, on numerical examples. In Section 3, we give examples illustrating the possible failure of the finite-information condition, as described in (C3), which occurs exceptionally in finite dimensions and frequently in infinite dimensions. In Section 4, we propose a non-probabilistic regularised autoencoder, FAE, as discussed in (C4), which applies even when the finite-information condition fails. We validate this approach on two examples taken from scientific machine learning—fluid flows governed by the Navier–Stokes equations, and pressure fields arising from subsurface flows—and make use of FAE’s mesh-invariance for the applications in (C5). In Section 5, we discuss related work, and in Section 6 we discuss limitations and topics for future research.

## 2 Variational Autoencoders on Function Space

VAEs are probabilistic models for dimension reduction and generative modelling using neural networks, based on an objective that jointly trains a generative model mapping Gaussian noise  $z$  to data  $u$  through a decoder neural network  $g$ , and performs variational inference to

approximate the distribution  $z | u$  using an encoder neural network  $f$ . Together, the maps  $f$  and  $g$  result in an autoencoder: an approximate factorisation of the identity mapping, factored through a low-dimensional latent space.

Compared to autoencoders in general, VAEs have the added benefit of regularising the latent space to be approximately Gaussian, which makes VAEs particularly suited to generative modelling and discovery of semantic structure in the data. The goal of this section is to develop a well-defined extension of the VAEs objective to function space, and to pair this objective with operator architectures that can be discretised at any resolution, resulting in a model we call the **functional variational autoencoder (FVAE)**.

In Section 2.1, we review the VAE objective in finite dimensions proposed by Kingma and Welling (2014), and in Section 2.2, we extend this objective to function space. Our key insight is to average the usual VAE objective over the data; this reveals an essential *finite-information condition* necessary for VAEs to be well-defined and that requires great care in infinite dimensions. In Section 2.3, we specialise our proposed objective to two settings where the finite-information condition is satisfied: path distributions of SDEs and Bayesian posteriors arising in inverse problems. In Section 2.4, we describe how to discretise the well-defined continuum objective, and complement this with encoder and decoder architectures based on neural operators, resulting in our proposed mesh-invariant FVAE. In Section 2.5, we validate our approach on several numerical examples.

## 2.1 Objective in Finite Dimensions

Let  $\mathcal{U} = \mathbb{R}^{d_u}$  and denote by  $\mathcal{P}(\mathcal{U})$  the set of Borel probability measures on  $\mathcal{U}$ . Assume that data are distributed according to the measure  $\Upsilon \in \mathcal{P}(\mathcal{U})$ , from which we observe finitely many samples. Fixing a **latent space**  $\mathcal{Z} = \mathbb{R}^{d_z}$ , typically with  $d_z \ll d_u$ , the starting point in the formulation of VAEs is to specify a generative model for  $u$  by specifying the distribution  $\mathbb{P}_z$  (with density  $p_z$ ) of the latent variable  $z \in \mathcal{Z}$  and the distribution  $\mathbb{P}_{u|z}$  (with density  $p_{u|z}$ ) of the conditional  $u | z$ . A common simplifying choice is

$$\begin{cases} u | z = g(z; \theta_g) + \eta, \\ z \sim \mathbb{P}_z := N(0, I_{d_z}), \\ \eta \sim \mathbb{P}_\eta := N(0, \frac{\beta}{2} I_{d_u}), \end{cases} \quad (2.1)$$

with the **decoder**  $g: \mathcal{Z} \times \Theta_g \rightarrow \mathcal{U}$  defined as a neural network parametrised by  $\theta_g \in \Theta_g$  and with  $\beta > 0$  fixed as a hyperparameter. The model (2.1) specifies a joint distribution on  $(z, u)$  with marginal densities  $p_z$  and  $p_u^{\theta_g}$ ; moreover, conditioning on  $u \in \mathcal{U}$  leads to a posterior  $z | u$  with density  $p_{z|u}^{\theta_g}$ . Here and in Section 2.2, we explicitly note the dependence of the measures and densities on the neural-network parameters except where there is no ambiguity. Since accessing  $z | u$  is typically intractable, VAEs perform variational inference with the **variational family**

$$\mathbb{Q}_{z|u}^{\theta_f} := N\left(m(u; \theta_f), \Sigma(u; \theta_f)\right), \quad u \in \mathcal{U} \quad (2.2)$$

having associated density  $q_{z|u}^{\theta_f}$ , with mean vector  $m(u; \theta_f) \in \mathcal{Z}$  and symmetric, positive-definite covariance matrix  $\Sigma(u; \theta_f) \in \mathcal{S}_+(\mathcal{Z})$  given by an **encoder** neural network  $f :=$



$(m, \Sigma): \mathcal{U} \times \Theta_f \rightarrow \mathcal{Z} \times \mathcal{S}_+(\mathcal{Z})$  parametrised by  $\theta_f \in \Theta_f$ . To derive an objective that jointly trains the generative model and performs variational inference, the log-marginal likelihood for data  $u \in \mathcal{U}$  under the model is written as

$$\log p_u^{\theta_g}(u) = D_{\text{KL}}(q_{z|u}^{\theta_f} \| p_{z|u}^{\theta_g}) + \mathcal{L}_{\text{VAE}}(u; \theta_f, \theta_g, \beta), \quad (2.3)$$

where we assume each term is finite and define  $\mathcal{L}_{\text{VAE}}(u; \theta_f, \theta_g, \beta)$  to be the evidence lower bound (ELBO) of Kingma and Welling (2014, eq. (3)), which takes, up to a finite constant  $C(\beta)$ , the form of a regularised misfit when  $u | z$  is Gaussian:

$$\mathcal{L}_{\text{VAE}}(u; \theta_f, \theta_g, \beta) = \mathbb{E}_{z \sim q_{z|u}^{\theta_f}} \left[ \log p_{u|z}^{\theta_g}(u) \right] - D_{\text{KL}}(q_{z|u}^{\theta_f} \| p_z) \quad (2.4a)$$

$$= \mathbb{E}_{z \sim q_{z|u}^{\theta_f}} \left[ -\beta^{-1} \|g(z; \theta_g) - u\|_2^2 \right] - D_{\text{KL}}(q_{z|u}^{\theta_f} \| p_z) + C(\beta). \quad (2.4b)$$

Under mild conditions on the data, maximising the ELBO (2.4b) over  $\theta_f$  and  $\theta_g$  (viewing  $\beta$  as a fixed hyperparameter) simultaneously performs variational inference and minimises the Kullback–Leibler (KL) divergence from the generative model  $p_u$  to the data distribution.

## 2.2 Well-Defined VAE Objective in Infinite Dimensions

Suppose now that  $\mathcal{U}$  is a (possibly infinite-dimensional) separable Banach space and, as before, assume data are distributed according to  $\Upsilon \in \mathcal{P}(\mathcal{U})$  and the latent space  $\mathcal{Z} = \mathbb{R}^{d_z}$ . Extending the formulation of VAEs to this setting necessitates several changes: the decoder noise  $\eta$  must now take values in the Banach space  $\mathcal{U}$ , and the expression (2.3) must be adapted to make sense in infinite dimensions, where measures do not have (Lebesgue) probability densities (Sudakov, 1959).

We argue that the appropriate generalisation of (2.3) and the ELBO (2.4) is to take expectations with respect to  $u \sim \Upsilon$  and consider the underlying *population loss*. Doing this reveals the conditions necessary to ensure that the underlying VAE objective is well-defined and finite—conditions not readily apparent under the per-sample viewpoint of (2.4). Proceeding similarly to the previous section, we take the generative model

$$\begin{cases} u | z = g(z; \theta_g) + \eta, \\ z \sim \mathbb{P}_z := N(0, I_{d_z}), \\ \eta \sim \mathbb{P}_\eta, \end{cases} \quad (2.5)$$

with the decoder noise measure  $\mathbb{P}_\eta$  now a centred nondegenerate Gaussian on  $\mathcal{U}$ . By this, we mean that whenever  $\ell$  is a continuous linear functional on  $\mathcal{U}$ , the scalar random variable  $\ell(\eta)$  has mean-zero, positive-variance Gaussian distribution (Bogachev, 1998). When  $\dim \mathcal{U} = \infty$ , there is no standard Gaussian distribution on  $\mathcal{U}$  with identity covariance, so the choice of  $\mathbb{P}_\eta$  becomes significant. We also assume the decoder  $g: \mathcal{Z} \times \Theta_g \rightarrow \mathcal{V} \subseteq \mathcal{U}$  may have range strictly smaller than  $\mathcal{U}$ , for reasons that we shall soon discuss.

The model (2.5) induces a joint measure  $\mathbb{P}_{z,u}^{\theta_g} \in \mathcal{P}(\mathcal{Z} \times \mathcal{U})$  that factorises in two ways: denoting by  $\mathbb{P}_{u|z}^{\theta_g}$  the distribution of  $u | z$  and by  $\mathbb{P}_{z|u}^{\theta_g}$  the distribution of  $z | u$ , we have

$$\mathbb{P}_{z,u}^{\theta_g}(dz, du) = \mathbb{P}_z(dz) \mathbb{P}_{u|z}^{\theta_g}(du), \quad (2.6)$$

$$\mathbb{P}_{z,u}^{\theta_g}(dz, du) = \mathbb{P}_{z|u}^{\theta_g}(dz) \mathbb{P}_u^{\theta_g}(du). \quad (2.7)$$

We again take the Gaussian variational family (2.2) with mean and covariance matrix parametrised by an encoder  $f := (m, \Sigma) : \mathcal{U} \times \Theta_f \rightarrow \mathcal{Z} \times \mathcal{S}_+(\mathcal{Z})$ , and define the approximate joint measure

$$\mathbb{Q}_{z,u}^{\theta_f}(dz, du) := \mathbb{Q}_{z|u}^{\theta_f}(dz)\Upsilon(du). \quad (2.8)$$

The observation motivating our training objective is that, while the expression (2.3) no longer makes sense as it is formulated in terms of Lebesgue probability densities, the true goal of a VAE is to maximise the ELBO *over a training dataset of samples*  $u \sim \Upsilon$ . In this setting the natural population loss with which to work is the KL divergence

$$\begin{aligned} D_{\text{KL}}(\mathbb{Q}_{z,u}^{\theta_f} \parallel \mathbb{P}_{z,u}^{\theta_g}) &:= \mathbb{E}_{(z,u) \sim \mathbb{Q}_{z,u}} \left[ \log \frac{d\mathbb{Q}_{z,u}}{d\mathbb{P}_{z,u}}(z, u; \theta_f, \theta_g) \right] \\ &= \mathbb{E}_{u \sim \Upsilon} \mathbb{E}_{z \sim \mathbb{Q}_{z|u}} \left[ \log \frac{d\mathbb{Q}_{z,u}}{d\mathbb{P}_{z,u}}(z, u; \theta_f, \theta_g) \right]. \end{aligned} \quad (2.9)$$

A necessary condition for this to be defined is that  $\mathbb{Q}_{z,u}^{\theta_f}$  is absolutely continuous with respect to  $\mathbb{P}_{z,u}^{\theta_g}$ , denoted  $\mathbb{Q}_{z,u}^{\theta_f} \ll \mathbb{P}_{z,u}^{\theta_g}$ , so that the density  $d\mathbb{Q}_{z,u}/d\mathbb{P}_{z,u}$  exists. The factorisations (2.6), (2.7), and (2.8) reveal that this is the case under a condition on the  $\mathcal{U}$ -marginals. Proofs for the results that follow are provided in Appendix A.1.

**Lemma 2.1** *Fix  $\theta_f \in \Theta_f$  and  $\theta_g \in \Theta_g$ , and suppose that  $\Upsilon \ll \mathbb{P}_{u|z}^{\theta_g}$  for all  $z \in \mathcal{Z}$ . Then  $\Upsilon \ll \mathbb{P}_u^{\theta_g}$  and  $\mathbb{Q}_{z,u}^{\theta_f} \ll \mathbb{P}_{z,u}^{\theta_g}$ , with*

$$\frac{d\mathbb{Q}_{z,u}}{d\mathbb{P}_{z,u}}(z, u; \theta_f, \theta_g) = \frac{d\Upsilon}{d\mathbb{P}_{u|z}}(u; \theta_g) \frac{d\mathbb{Q}_{z|u}}{d\mathbb{P}_z}(z; \theta_f) = \frac{d\Upsilon}{d\mathbb{P}_u}(u; \theta_g) \frac{d\mathbb{Q}_{z|u}}{d\mathbb{P}_{z|u}}(z; \theta_f, \theta_g).$$

We shall see that the hypothesis of Lemma 2.1 is satisfied under our formulation given a condition on the data measure  $\Upsilon$  and the decoder range  $\mathcal{V}$ . Before stating this, let us suppose further that the divergence (2.9) is finite. In this case, we obtain a natural extension of the expression (2.3), justifying the interpretation of (2.9) as the population loss for VAEs.

**Theorem 2.2** *Fix  $\theta_f \in \Theta_f$  and  $\theta_g \in \Theta_g$ , and suppose  $\Upsilon \ll \mathbb{P}_{u|z}^{\theta_g}$  for all  $z \in \mathcal{Z}$  and  $D_{\text{KL}}(\mathbb{Q}_{z,u}^{\theta_f} \parallel \mathbb{P}_{z,u}^{\theta_g}) < \infty$ . Then*

$$-D_{\text{KL}}(\Upsilon \parallel \mathbb{P}_u^{\theta_g}) = \mathbb{E}_{u \sim \Upsilon} \left[ D_{\text{KL}}(\mathbb{Q}_{z|u}^{\theta_f} \parallel \mathbb{P}_{z|u}^{\theta_g}) \right] - D_{\text{KL}}(\mathbb{Q}_{z,u}^{\theta_f} \parallel \mathbb{P}_{z,u}^{\theta_g}). \quad (2.10)$$

The equality (2.10) is indeed the extension of (2.3), since the expectation of the log-likelihood  $\log p_u^{\theta_g}(u)$  over  $u \sim \Upsilon$  is, up to a constant, equal to  $-D_{\text{KL}}(\Upsilon \parallel \mathbb{P}_u^{\theta_g})$ . This equality forms the foundation of a tractable objective under the additional assumptions that both  $\mathbb{P}_{u|z}^{\theta_g} \ll \mathbb{P}_\eta$  for all  $z \in \mathcal{Z}$  and a **finite-information condition** that  $D_{\text{KL}}(\Upsilon \parallel \mathbb{P}_\eta) < \infty$  holds; henceforth, we write

$$\mathcal{P}(\mathcal{U} \parallel \mathbb{P}_\eta) := \{ \mu \in \mathcal{P}(\mathcal{U}) \mid D_{\text{KL}}(\mu \parallel \mathbb{P}_\eta) < \infty \}.$$

**Theorem 2.3 (ELBO under finite-information condition)** Fix  $\theta_f \in \Theta_f$ ,  $\theta_g \in \Theta_g$ , and  $\Upsilon \in \mathcal{P}(\mathcal{U} \parallel \mathbb{P}_\eta)$ . Suppose  $\Upsilon \ll \mathbb{P}_{u|z}^{\theta_g} \ll \mathbb{P}_\eta$  for all  $z \in \mathcal{Z}$  and  $D_{\text{KL}}(\mathbb{Q}_{z,u}^{\theta_f} \parallel \mathbb{P}_{z,u}^{\theta_g}) < \infty$ . Then

$$D_{\text{KL}}(\mathbb{Q}_{z,u}^{\theta_f} \parallel \mathbb{P}_{z,u}^{\theta_g}) = \mathbb{E}_{u \sim \Upsilon} [-\mathcal{L}(u; \theta_f, \theta_g)] + D_{\text{KL}}(\Upsilon \parallel \mathbb{P}_\eta), \quad (2.11)$$

$$\mathcal{L}(u; \theta_f, \theta_g) := \mathbb{E}_{z \sim \mathbb{Q}_{z|u}^{\theta_f}} \left[ \log \frac{d\mathbb{P}_{u|z}}{d\mathbb{P}_\eta}(u; \theta_g) \right] - D_{\text{KL}}(\mathbb{Q}_{z|u}^{\theta_f} \parallel \mathbb{P}_z). \quad (2.12)$$

This result naturally suggests a practical continuum training objective which corresponds, up to a finite constant, to the population loss  $D_{\text{KL}}(\mathbb{Q}_{z,u}^{\theta_f} \parallel \mathbb{P}_{z,u}^{\theta_g})$ :

$$\mathcal{J}(\theta_f, \theta_g) := \mathbb{E}_{u \sim \Upsilon} [-\mathcal{L}(u; \theta_f, \theta_g)]. \quad (2.13)$$

Indeed, it is reasonable to seek to minimise  $\mathcal{J}$  since its infimum over the parameters  $\theta_f$  and  $\theta_g$  is finite if  $\Upsilon \in \mathcal{P}(\mathcal{U} \parallel \mathbb{P}_\eta)$  and there exist  $\theta_f \in \Theta_f$  and  $\theta_g \in \Theta_g$  such that

$$f(u; \theta_f) = (0, I_{d_{\mathcal{Z}}}), \quad u \in \mathcal{U}, \quad g(z; \theta_g) = 0, \quad z \in \mathcal{Z}.$$

In other words, under this condition on  $\Theta_f$  and  $\Theta_g$ , we know that the loss function is finite at at least one point. Let us now address the question of whether  $\Upsilon \ll \mathbb{P}_{u|z} \ll \mathbb{P}_\eta$  for all  $z \in \mathcal{Z}$ . Since we must assume in Theorem 2.3 that  $\Upsilon \in \mathcal{P}(\mathcal{U} \parallel \mathbb{P}_\eta)$  to obtain a practical objective, it is certainly the case that  $\Upsilon \ll \mathbb{P}_\eta$ . But thanks to the **Cameron–Martin theorem** (Bogachev, 1998, Corollary 2.4.3), the shift  $\mathbb{P}_{u|z} = \mathbb{P}_\eta(\cdot - g(z; \theta_g))$  is equivalent in the sense of measures to  $\mathbb{P}_\eta$ , i.e.,  $\mathbb{P}_{u|z} \ll \mathbb{P}_\eta$  and  $\mathbb{P}_\eta \ll \mathbb{P}_{u|z}$ , provided the decoder range  $\mathcal{V}$  is a subset of the **Cameron–Martin space**  $H(\mathbb{P}_\eta) \subset \mathcal{U}$  associated with the Gaussian measure  $\mathbb{P}_\eta$ . Under this assumption on  $\mathcal{V}$ , it thus follows that  $\Upsilon \ll \mathbb{P}_{u|z}$  for all  $z \in \mathcal{Z}$ .

Before stating the theorem, we recall the following relevant facts from Gaussian measure theory. The space  $H(\mathbb{P}_\eta)$  is Hilbert, and for fixed  $h \in H(\mathbb{P}_\eta)$ , the  $H(\mathbb{P}_\eta)$ -inner product  $\langle h, \cdot \rangle_{H(\mathbb{P}_\eta)}$  extends uniquely (up to equivalence  $\mathbb{P}_\eta$ -almost everywhere) to a *measurable linear functional* (Bogachev, 1998, Theorem 2.10.11), which we denote  $u \in \mathcal{U} \mapsto \langle h, u \rangle_{H(\mathbb{P}_\eta)}$ .

**Proposition 2.4 (Cameron–Martin theorem)** Let  $\mu_0 \in \mathcal{P}(\mathcal{U})$  be a Gaussian measure with Cameron–Martin space  $H(\mu_0)$ , let  $h \in \mathcal{U}$ , and suppose that  $\mu^h := \mu_0(\cdot - h)$  is the shift of  $\mu_0$  by  $h$ . Then  $\mu^h$  is equivalent if  $h \in H(\mu_0)$ , and

$$\mu^h(du) = \exp\left(\langle h, u \rangle_{H(\mu_0)} - \frac{1}{2} \|h\|_{H(\mu_0)}^2\right) \mu_0(du). \quad (2.14)$$

Otherwise,  $\mu^h$  and  $\mu_0$  are mutually singular, i.e.,  $\mu^h \not\ll \mu_0$  and  $\mu_0 \not\ll \mu^h$ , denoted  $\mu^h \perp \mu_0$ .

Consequently, we shall assume throughout that  $\mathcal{V} := H(\mathbb{P}_\eta)$ , so that, as a result of the Cameron–Martin formula (2.14), the ELBO  $\mathcal{L}(u; \theta_f, \theta_g)$  may be written as

$$\mathcal{L}(u; \theta_f, \theta_g) = \mathbb{E}_{z \sim \mathbb{Q}_{z|u}^{\theta_f}} \left[ \langle g(z; \theta_g), u \rangle_{H(\mathbb{P}_\eta)} - \frac{1}{2} \|g(z; \theta_g)\|_{H(\mathbb{P}_\eta)}^2 \right] - D_{\text{KL}}(\mathbb{Q}_{z|u}^{\theta_f} \parallel \mathbb{P}_z). \quad (2.15)$$

**Remark 2.5** (a) Applying the reparametrisation trick (Kingma and Welling, 2014) and writing out the KL divergence on the latent space analytically makes the interpretation of the objective  $\mathcal{J}(\theta_f, \theta_g)$  as that of a regularised autoencoder more obvious:

$$\mathcal{J}(\theta_f, \theta_g) = \mathbb{E}_{\substack{u \sim \Upsilon \\ \xi \sim \mathbb{P}_z}} \left[ \mathcal{M} \left( g \left( m(u; \theta_f) + \Sigma(u; \theta_f) \xi; \theta_g \right), u \right) + \mathcal{R}(u; \theta_f) \right],$$

where the **misfit term**  $\mathcal{M}(h, u)$  is given by

$$\mathcal{M}(h, u) := \frac{1}{2} \|h\|_{H(\mathbb{P}_\eta)}^2 - \langle h, u \rangle_{\tilde{H}(\mathbb{P}_\eta)},$$

and the **regularisation term**  $\mathcal{R}(u; \theta_f)$  is given by

$$\mathcal{R}(u; \theta_f) := \frac{1}{2} \|m(u; \theta_f)\|_2^2 + \frac{1}{2} \text{tr}(\Sigma(u; \theta_f) - \log \Sigma(u; \theta_f)) - \frac{d_z}{2}.$$

The term  $\mathcal{M}(h, u)$  can be seen as the mean-squared error (MSE)  $\frac{1}{2} \|h - u\|_{H(\mathbb{P}_\eta)}^2$  with the almost-surely-infinite term  $\frac{1}{2} \|u\|_{H(\mathbb{P}_\eta)}^2$  subtracted (see Stuart, 2010, Remark 3.8).

(b) The requirement that  $D_{\text{KL}}(\Upsilon \parallel \mathbb{P}_\eta) < \infty$  is not unique to the infinite-dimensional setting. In finite dimensions, however, the failure of these conditions is “exceptional”, whereas in infinite dimensions it is typical: even insisting  $\Upsilon \ll \mathbb{P}_\eta$  is a very stringent condition. We discuss this issue in more detail in Section 3.

## 2.3 Applications

We now give two practical examples of settings for which it is possible to apply our methodology, arising in the study of random dynamical systems (Section 2.3.1) and in Bayesian inverse problems (Section 2.3.2). In both cases, the structure of the data distribution ensures that there is a known Gaussian measure  $\mathbb{P}_\eta$  such that the finite-information condition  $\Upsilon \in \mathcal{P}(\mathcal{U} \parallel \mathbb{P}_\eta)$  holds, and the properties of the decoder noise measure  $\mathbb{P}_\eta$  dictate the form of the resulting training objective.

### 2.3.1 STOCHASTIC DIFFERENTIAL EQUATIONS

In this subsection, we focus on the random dynamical systems setting (e.g., E et al., 2004) and assume that  $\Upsilon$  is the distribution of sample paths of the  $\mathbb{R}^m$ -valued diffusion

$$du_t = b(u_t) dt + \sqrt{\varepsilon} dw_t, \quad u_0 = 0, \quad t \in [0, T], \quad (2.16)$$

where  $(w_t)_{t \in [0, T]}$  is a Brownian motion on  $\mathbb{R}^m$ . We take  $\varepsilon > 0$  and assume that the drift function  $b: \mathbb{R}^m \rightarrow \mathbb{R}^m$  possesses sufficient regularity for (2.16) to be well defined. The theory we outline applies more generally to systems with anisotropic diffusion and time-dependent coefficients (Särkkä and Solin, 2019, Sec. 7.3), but we focus on the setting (2.16) to simplify the exposition. The measure  $\Upsilon$  is defined on the space  $\mathcal{U} = C_0([0, T], \mathbb{R}^m)$  of continuous functions  $u(t)$  with  $u(0) = 0$ , and we shall take the decoder noise measure  $\mathbb{P}_\eta$  to be the distribution of the modified SDE

$$dv_t = c(v_t) dt + \sqrt{\varepsilon} dw_t, \quad v_0 = 0, \quad t \in [0, T], \quad (2.17)$$

with drift  $c: \mathbb{R}^m \rightarrow \mathbb{R}^m$  and with  $\varepsilon > 0$  being the same as in (2.16). Our formulation of the FVAE objective assumed that  $\mathbb{P}_\eta$  was Gaussian and  $\Upsilon \in \mathcal{P}(\mathcal{U} \parallel \mathbb{P}_\eta)$ ; these conditions can be verified with the aid of the Girsanov theorem (see, e.g., Liptser and Shiryaev, 2001, Chap. 7). Indeed, under specific choices of  $c$ , the decoder noise  $\eta$  is Gaussian on  $\mathcal{U}$ , and the Girsanov formula yields the density  $d\mathbb{P}_{u|z}/d\mathbb{P}_\eta$  needed in the ELBO (2.15):

- (a)  $c(x, t) = 0$ , resulting in  $\mathbb{P}_\eta$  being the Wiener measure, i.e., the law of a Brownian motion on  $\mathbb{R}^m$ , for which

$$-\log \frac{d\mathbb{P}_{u|z}}{d\mathbb{P}_\eta}(u) = \frac{1}{2\varepsilon} \int_0^T \|h'(t)\|_2^2 dt - \frac{1}{\varepsilon} \int_0^T h'(t) du_t, \quad (2.18)$$

where the latter integral is an Itô stochastic integral (see Särkkä and Solin, 2019).

- (b)  $c(x, t) = -\theta x$  for some constant  $\theta > 0$ , resulting in  $\mu_0$  being the law of a  $\theta$ -Ornstein–Uhlenbeck (OU) process, for which  $H(\mu_0)$  again consists of  $H^1$ -functions with  $u(0) = 0$ , and, thanks to the Girsanov formula (Øksendal, 2003)

$$-\log \frac{d\mathbb{P}_{u|z}}{d\mathbb{P}_\eta}(u) = \frac{1}{\varepsilon} \int_0^T \frac{1}{2} \|h'(t)\|_2^2 - \theta \langle h'(t), u(t) \rangle dt - \frac{1}{\varepsilon} \int_0^T h'(t) du_t. \quad (2.19)$$

The finite-information condition  $\Upsilon \in \mathcal{P}(\mathcal{U} \parallel \mathbb{P}_\eta)$  is satisfied under relatively mild conditions on  $b$  and  $c$  (Lemma A.1), with the resulting KL divergence given by

$$D_{\text{KL}}(\Upsilon \parallel \mathbb{P}_\eta) = \mathbb{E}_{u \sim \Upsilon} \left[ \frac{1}{2\varepsilon} \int_0^T \|b(u_t) - c(u_t)\|_2^2 \right];$$

this divergence is obviously finite if, for example,  $b$  and  $c$  are bounded. To ensure that  $g(z; \theta_g)(0) \approx 0$ , we add a further **zero-penalty term** with scale  $\lambda > 0$ , and we add a **regularisation scale**  $\beta > 0$  to better control the strength of the regularisation, leading to the training objective

$$\mathcal{J}_{\text{SDE}}(\theta_f, \theta_g, \lambda, \beta) := \mathbb{E}_{u \sim \Upsilon} \left[ \mathbb{E}_{z \sim \mathbb{Q}_{z|u}} \left[ -\log \frac{d\mathbb{P}_{u|z}}{d\mathbb{P}_\eta}(u) + \lambda \|g(z; \theta_g)(0)\|_2^2 \right] + \beta D_{\text{KL}}(\mathbb{Q}_{z|u} \parallel \mathbb{P}_z) \right]. \quad (2.20)$$

We enforce that  $g(z; \theta_g)$  lies in the Cameron–Martin space  $H(\mathbb{P}_\eta)$  implicitly: if  $g(z; \theta_g) \notin H(\mathbb{P}_\eta)$ , then at least one of the terms in the loss (2.20) is infinite. This objective extends naturally to the case that the underlying data SDE (2.16) has nonzero initial condition  $u_0$  by translating the data by  $-u_0$  and shifting the decoded function  $g(z; \theta_g)$  by  $u_0$  so that realisations from the FVAE generative model have (approximate) initial condition  $u_0$ .

### 2.3.2 BAYESIAN INVERSE PROBLEMS

Another case in which the structure of the data measure suggests an appropriate decoder noise measure arises in the study of Bayesian inverse problems (Stuart, 2010). We exemplify this setting with a simple additive-noise Bayesian inverse problem. Let  $\mathcal{U}$  be a separable Hilbert space, let  $Y = \mathbb{R}^{d_Y}$ , and let  $\mathcal{G}: \mathcal{U} \rightarrow Y$  be a (possibly nonlinear) **observation operator**. Suppose that  $y \in Y$  is given by the model

$$y = \mathcal{G}(u) + \xi, \quad u \sim \mu_0, \quad \xi \sim N(0, \Sigma), \quad (2.21)$$

with noise covariance  $\Sigma \in \mathcal{S}_+(Y)$ , and with **prior measure**  $\mu_0 = N(0, C)$  having covariance operator  $C: \mathcal{U} \rightarrow \mathcal{U}$ . Models of this type arise, for example, in Lagrangian data assimilation problems in oceanography (Cotter et al., 2010). Given an observation  $y \in Y$  from the model (2.21), the Bayesian approach seeks to infer the unknown  $u \in \mathcal{U}$  by computing the posterior measure  $\mu^y$  on  $\mathcal{U}$ , representing the distribution of  $u \mid y$ . In the setting of (2.21), the posterior  $\mu^y$  has a density with respect to the prior  $\mu_0$  thanks to Bayes’ rule (e.g., Dashti and Stuart, 2017, Theorem 14), taking the form

$$\frac{d\mu^y}{d\mu_0}(u) = \frac{1}{Z(y)} \exp(-\Phi(u; y)), \quad \Phi(u; y) = \frac{1}{2} \|\mathcal{G}(u) - y\|_\Sigma^2, \quad \|\cdot\|_\Sigma = \|\Sigma^{-1/2} \cdot\|_2,$$

where  $Z(y) \in (0, 1]$  owing to the nonnegativity of  $\Phi$ . A simple calculation then reveals

$$D_{\text{KL}}(\mu^y \parallel \mu_0) = \mathbb{E}_{u \sim \mu^y} \left[ \log \frac{d\mu^y}{d\mu_0}(u) \right] = \mathbb{E}_{u \sim \Upsilon} [-\log Z(y) - \Phi(u)] \leq -\log Z(y) < \infty.$$

Consequently,  $\mu^y \in \mathcal{P}(\mathcal{U} \parallel \mu_0)$ , and our FVAE objective can be applied to data from the posterior  $\mu^y$ , taking the Gaussian prior  $\mu_0$  as the decoder noise  $\mathbb{P}_\eta$ . In this Hilbert setting,  $H(\mathbb{P}_\eta) = C^{1/2}\mathcal{U}$ , and the norm and inner product in (2.15) admit the simple form

$$\|h\|_{H(\mathbb{P}_\eta)} = \|C^{-1/2}h\|_{\mathcal{U}}, \quad \langle h, u \rangle_{H(\mathbb{P}_\eta)} = \langle C^{-1/2}h, C^{-1/2}u \rangle_{\mathcal{U}}, \quad h \in H(\mathbb{P}_\eta), \quad u \in \mathcal{U}.$$

Similar arguments apply quite generally for observation models other than (2.21), provided the resulting log-density  $\log d\mu^y/d\mu_0$  satisfies suitable boundedness or integrability conditions. In any case, provided the finite-information condition  $\mu^y \in \mathcal{P}(\mathcal{U} \parallel \mu_0)$  holds, we may specialise the training objective to obtain

$$\mathcal{J}_{\text{BIP}}(\theta_f, \theta_g) = \mathbb{E}_{u \sim \Upsilon} \left[ \mathbb{E}_{z \sim \mathbb{Q}_{z|u}} \left[ \frac{1}{2} \|C^{-1/2}g(z; \theta_g)\|_{\mathcal{U}}^2 - \langle C^{-1/2}g(z; \theta_g), C^{-1/2}u \rangle_{\mathcal{U}} \right] + D_{\text{KL}}(\mathbb{Q}_{z|u} \parallel \mathbb{P}_z) \right].$$

This methodology could be used to generate further approximate samples from the posterior, taking as data the output of a function-space MCMC method (Cotter et al., 2013).

## 2.4 Architecture and Algorithms

After establishing the well-defined FVAE objective on function space (Section 2.2) and concrete settings for which the objective applies (Section 2.3), the remaining tasks are to discretise the losses and to parametrise the encoder and decoder with learnable mappings that can be evaluated on any mesh.

Our framework has the flexibility to use a wide variety of neural operators in the encoder and decoder, including DeepONet (Lu et al., 2021) and Fourier neural operators (Kovachki et al., 2023). We focus on architectures allowing both the encoder and decoder to be discretised on arbitrary meshes; as we shall discuss in Section 2.5, there is significant benefit in being able to use distinct meshes in the encoder and decoder.

We propose a common architecture to be used across all numerical experiments, focussing on the simplest method which remains competitive with more sophisticated neural-network architectures in order to concentrate on our methodological contributions. Our proposal bears similarities with existing operator architectures in the literature, such as

the variable-input DeepONet (VIDON; Prasthofer et al., 2022) and the nonlinear manifold decoder (NOMAD; Seidman et al., 2022). We also take inspiration from architectures for point-cloud data, e.g., PointNet (Qi et al., 2017). As in Section 2.3, we assume that  $\mathcal{U}$  is a Banach space of functions with domain  $\Omega \subseteq \mathbb{R}^d$  and range  $\mathbb{R}^m$ ; we further assume that functions  $u \in \mathcal{U}$  are evaluable pointwise.

In Section 2.4.1, we discuss the discrete approximation of the objectives derived in the previous subsection. In Section 2.4.2 and Section 2.4.3, we propose mesh-invariant architectures for the encoder and decoder inspired by existing function-to-vector and vector-to-function maps based on neural operators. In Section 2.4.4, we exploit the possibility of discretising the encoder and decoder on different meshes to propose a self-supervised training scheme with the aim of improving robustness to changes of mesh.

### 2.4.1 DISCRETISED LOSSES

For numerical implementation, the ELBO (2.12) must be discretised to allow computation of the expectations over  $\Upsilon$  and  $\mathbb{Q}_{z|u}$ , and of the function-space norms and inner products.

**Discretisation of expectations.** The expectation over  $u \sim \Upsilon$  is empiricalised by taking the mean over the (finite) training dataset. Following Kingma and Welling (2014), the expectation over  $z \sim \mathbb{Q}_{z|u}$  is approximated by Monte Carlo sampling, with the number of samples treated as a hyperparameter of the model.

**Discretisation of function-space norms.** In practice, data consists of discrete representations of functions  $u: \Omega \rightarrow \mathbb{R}^m$ , possibly on heterogeneous and irregular meshes, and we must discretise the continuum training objectives derived in Section 2.3 for numerical implementation. In the case that  $\mathcal{U}$  is Hilbert, it is often natural to represent the data as coefficients of an orthonormal basis, and thus the norms and inner products can be simply approximated by truncated sums. Frequently, however,  $\mathcal{U}$  is a space of functions and the norms and inner products can be viewed as integral functionals of the data, e.g., the  $L^2$ -inner product

$$\langle f, g \rangle_{L^2} = \int_{\Omega} f(x)g(x) dx,$$

and in this setting it is natural to approximate the integral through the normalised sum.

**Computing decoder derivatives with automatic differentiation.** In the objective derived in Section 2.3.1, terms involving the derivative  $g(z; \theta_g)'(t)$  with respect to the time variable arise frequently. As we shall parametrise  $g(z; \theta_g)$  as a differentiable neural network, it is natural to compute this derivative using automatic differentiation. This offers significant advantages over finite-difference approximation of the derivative in terms of numerical stability, and we adopt this strategy throughout the following numerical experiments.

**Approximation of stochastic integrals.** For the Itô stochastic integrals arising in Section 2.3.1, we discretise on the partition  $0 = t_0 < t_1 < \dots < t_n = T$  with

$$\int_0^T g(z; \theta_g)'(t)^T du_t \approx \sum_{j=1}^n g(z; \theta_g)'(t_{j-1})^T (u(t_j) - u(t_{j-1})).$$

This converges in probability to the stochastic integral (Särkkä and Solin, 2019, eq. (4.6)).

### 2.4.2 ENCODER ARCHITECTURE

At the function-space level, the encoder is a parametrised mapping taking an input function  $u: \Omega \rightarrow \mathbb{R}^m$  to the mean vector  $m(u; \theta_f) \in \mathcal{Z}$  and covariance matrix  $\Sigma(u; \theta_f) \in \mathcal{S}_+(\mathcal{Z})$  of the Gaussian variational distribution  $\mathbb{Q}_{z|u}^{\theta_f}$  on the latent space  $\mathcal{Z}$ :

$$f := (m, \Sigma): \mathcal{U} \times \Theta_f \rightarrow \mathcal{Z} \times \mathcal{S}_+(\mathcal{Z}).$$

As is typical for VAEs, we assume  $\Sigma(u; \theta_f)$  is a diagonal matrix for all  $u \in \mathcal{U}$  and write

$$f(u; \theta_f) = \left( \tilde{f}_1(u; \theta_f), \text{diag}(\exp(\tilde{f}_2(u; \theta_f))) \right)$$

for some parametrised function-to-vector map  $\tilde{f} := (\tilde{f}_1, \tilde{f}_2): \mathcal{U} \times \Theta_f \rightarrow \mathbb{R}^{d_z} \times \mathbb{R}^{d_z} = \mathbb{R}^{2d_z}$ . We define  $\tilde{f}$  as an integration of the learnable vector-valued kernel  $\kappa: \Omega \times \mathbb{R}^m \times \Theta_f \rightarrow \mathbb{R}^\ell$ , followed by the learnable mapping  $\rho: \mathbb{R}^\ell \times \Theta_f \rightarrow \mathbb{R}^{2d_z}$ :

$$\tilde{f}(u; \theta_f) = \rho \left( \int_{\Omega} \kappa(x, u(x); \theta_f) dx; \theta_f \right). \quad (2.22)$$

We parametrise  $\kappa$  as a neural network with 2 hidden layers and output dimension  $\ell = 64$ , using GELU activation (Hendrycks and Gimpel, 2016), and we parametrise  $\rho$  as the linear layer  $\rho(x; \theta_f) = Wx + b$ , with  $W \in \mathbb{R}^{2d_z \times \ell}$  and  $b \in \mathbb{R}^{2d_z}$ . We augment the coordinate  $x \in \Omega$  in  $\kappa$  with 16 random Fourier features (Tancik et al., 2020) as described in Appendix B.1 to aid learning of high-frequency features in the integral kernel; this proves essential given the pivotal role of the kernel in our architecture.

Given a function  $u$  discretised on the mesh  $\{x_i\}_{i=1}^n$ , the integral in (2.22) is approximated as a normalised sum, resembling learnable set-to-vector maps proposed under various names, e.g., deep sets (Zaheer et al., 2017), PointNets (Qi et al., 2017), and statistic networks (Edwards and Storkey, 2017), all of which take the form

$$\{(x_i, u(x_i)) \mid i = 1, 2, \dots, n\} \mapsto \rho \left( \text{pool} \left( \{ \kappa(x_i, u(x_i)) \mid i = 1, 2, \dots, n \} \right) \right),$$

where pool is a pooling operation such as the mean; our approach differs from these works by taking the continuum formulation as the starting point. Related ideas from machine learning on sets, such as transformers (Vaswani et al., 2017), have already been applied to operator learning—e.g., the VIDON (Prasthofer et al., 2022), the mesh-independent neural operator (Lee, 2022), and continuum attention (Calvello et al., 2024). We believe there is great potential in extending other point-cloud and set architectures to the continuum limit.

At the function-space level, our encoder bears similarities with the linear-functional layer used in Fourier neural mappings (Huang et al., 2024) and the neural functional of Rahman et al. (2022). Our approach differs by allowing  $\kappa$  to depend on  $u$ , and by computing the integral in physical space. The distinct advantage of our approach is the ability to encode on any mesh, in contrast to approaches based on convolutions and the fast Fourier transform, which are largely limited to grids. We investigated the possibility of preceding (2.22) with a neural operator mapping between functions as in the work of Huang et al. (2024) and Rahman et al. (2022), but found no advantage on the datasets we consider.



### 2.4.3 DECODER ARCHITECTURE

The decoder, at the continuum, is a parametrised vector-to-function map taking a latent vector  $z \in \mathcal{Z}$  to a function  $g(z; \theta_g): \Omega \rightarrow \mathbb{R}^m$  in the Cameron–Martin space  $\mathcal{V} = H(\mathbb{P}_\eta)$ :

$$g: \mathcal{Z} \times \Theta_g \rightarrow H(\mathbb{P}_\eta).$$

Several approaches exist in the literature to parametrise vector-to-function mappings, and we briefly summarise. Huang et al. (2024) propose to lift the input vector to a function through multiplication with a learnable constant function, and then apply operator architectures such as FNO. Seidman et al. (2023) propose both a DeepONet-inspired decoder based on a linear combination of learnable basis functions, and a nonlinear decoder essentially the same as what we propose, which is also closely related to the architecture adopted by the NOMAD model. There can be significant benefits to embedding known structure in the decoder architecture but, for simplicity, we parametrise the decoder using a coordinate neural network  $\gamma: \mathcal{Z} \times \Omega \times \Theta_g \rightarrow \mathbb{R}^m$  with 5 hidden layers of width 100 using GELU activation throughout, so that

$$g(z; \theta_g)(x) = \gamma(z, x; \theta_g). \tag{2.23}$$

As before, we augment  $x \in \Omega$  with 16 random Fourier features (Appendix B.1) to allow  $\gamma$  to more easily capture high-frequency features. While we impose no smoothness requirement at the architectural level, the training objective (2.13) implicitly ensures that  $g(z; \theta_g)$  is smooth enough to lie in  $H(\mathbb{P}_\eta)$ : if  $g(z; \theta_g) \notin H(\mathbb{P}_\eta)$ , at least one term in the loss is infinite.

Our proposed architecture allows discretisation of the decoded function  $g(z; \theta_g)$  on any mesh, and the cost of evaluating the decoder (2.23) grows linearly with the number of mesh points. Moreover, queries at each coordinate  $x \in \Omega$  can be readily computed in parallel.

The use of coordinate neural networks is closely related to the literature on implicit neural representations (see, e.g., Sitzmann et al., 2020), in which one regresses on a fixed image using a coordinate neural network, treating the resulting weights as a resolution-independent representation of the underlying data.

### 2.4.4 SELF-SUPERVISED TRAINING

The strategy of **self-supervised learning**—learning to predict the missing data from a masked input—has proven valuable in both language models such as BERT (Devlin et al., 2019) and vision models such as the masked autoencoder (MAE; He et al., 2022), yielding benefits such as reduced training time and improved generalisation.

After dividing input images into patches, MAE encodes the data with 75% of patches removed, decoding only the patches which were unseen at encoding time. Since we can discretise the encoder and decoder on arbitrary distinct meshes, we propose a very natural extension of this idea: mask both the input mesh on which the encoder is discretised and the output mesh on which the decoder is discretised.

We chiefly focus on the MAE-inspired strategy of masking a fixed proportion of mesh points in the input, randomly selected at each batch, and decoding only on the masked points, but many other strategies are also possible, such as masking with polygons. We explore the computational tradeoffs of various masking strategies in Section 4.3.

We argue that self-supervised training is of particular value for resolution-invariant architectures: masking prevents the model from overfitting to the training mesh, leading to demonstrable benefits on tasks involving changes of mesh (Section 4.3.1).

## 2.5 Numerical Experiments

We apply our proposed FVAE on two examples where  $\Upsilon$  is an SDE path measure. These examples serve as prototypes for more complex problems in science and engineering, motivated by applications such as molecular dynamics (MD). For all experiments, we adopt the architecture described in Section 2.4. A summary of the conclusions to be drawn from the numerical experiments with these examples is as follows:

- (a) FVAE accurately captures pathwise and ensemble properties of the underlying data, with the learned latent variables having physically relevant meaning (Section 2.5.1);
- (b) choosing a decoder noise process that accurately reflects the stochastic variability in the data is essential to obtain a high-quality generative model (Section 2.5.1);
- (c) FVAE is robust to changes of mesh in the encoder and decoder, enabling training with heterogeneous data and principled generative modelling at any resolution, backed up by a well-defined probabilistic model (Section 2.5.2).

### 2.5.1 BROWNIAN DYNAMICS

The Brownian dynamics model (see Schlick, 2010, Chapter 14), also known as the Langevin model, is a stochastic approximation of deterministic Newtonian models for MD. In this model, the configuration  $u_t$  (in some configuration space  $X \subseteq \mathbb{R}^m$ ) of a molecule is assumed to follow the gradient flow of a **potential**  $U: X \rightarrow \mathbb{R}$  perturbed by additive thermal noise with **temperature**  $\varepsilon > 0$ , described by the Langevin SDE

$$du_t = -\nabla U(u_t) dt + \sqrt{\varepsilon} dw_t, \quad t \in [0, T], \quad (2.24)$$

where  $(w_t)_{t \in [0, T]}$  is a Brownian motion on  $\mathbb{R}^m$ .

As a prototype for the more sophisticated, high-dimensional potential functions arising in MD, such as the Lennard–Jones potential (see Schlick, 2010), we take  $X = \mathbb{R}$  and consider a one-dimensional asymmetric double-well potential given by

$$U(x) \propto 3x^4 - 2x^3 - 6x^2 + 6x. \quad (2.25)$$

This potential has a local minimum at  $x_1 = -1$  and a global minimum at  $x_2 = 1$  (Figure 2.1(a)). As discussed in Section 2.3.1, we internally translate by the initial condition  $u_0 = x_1$  so that the FVAE generative model approximately matches the true initial condition. We take  $\Upsilon$  be the distribution of the untranslated paths, with temperature  $\varepsilon = 1$ , final time  $T = 5$ , and initial condition  $u_0 = x_1$ . The training dataset consists of 8,192 paths with timestep  $5/512$  in  $[0, T]$ , where it is assumed that each sample path has 50% of timesteps missing; data are generated using an Euler–Maruyama solver as described in Appendix B.2.

Sample paths drawn from  $\Upsilon$  start at  $x_1$  and transition with very high probability to the potential-minimising state  $x_2$ ; the time at which the transition begins is determined by the thermal noise, but, once the transition has begun, the manner in which the transition

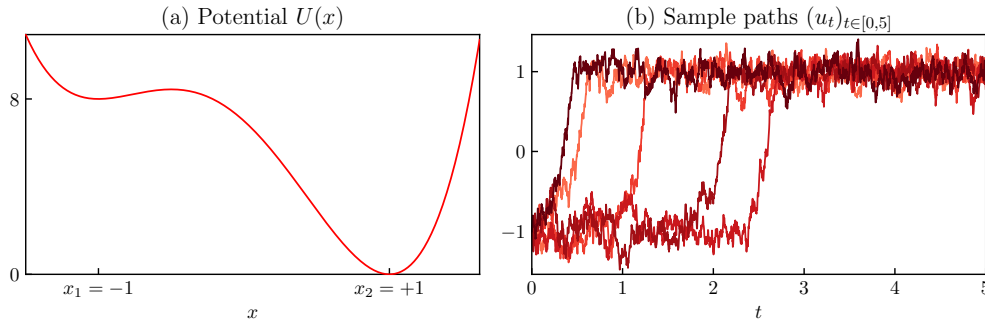


Figure 2.1: (a) Realisations of the SDE (2.24) follow the gradient flow of the potential  $U$ . (b) Sample paths  $(u_t)_{t \in [0, T]} \sim \Upsilon$  begin at  $x_1 = -1$  and transition with high probability to the lower-potential state  $x_2 = +1$  as a result of the additive thermal noise.

occurs is largely consistent across realisations. Such phenomena occur quite generally in the study of random dynamical systems and large-deviation theory (e.g., E et al., 2004).

We train FVAE using the SDE loss (Section 2.3.1) with regularisation scale  $\beta = 1$  and zero-penalty scale  $\lambda = 10$ , using several choices of decoder-noise measure  $\mathbb{P}_\eta$ . Motivated by the observation that the trajectories are determined chiefly by the transition time, we use latent dimension  $d_Z = 1$ .

**Choice of noise process  $\eta$ .** As discussed in Section 2.3.1, the choice of SDE (2.17) for the noising process  $\eta$  greatly affects the performance of FVAE.

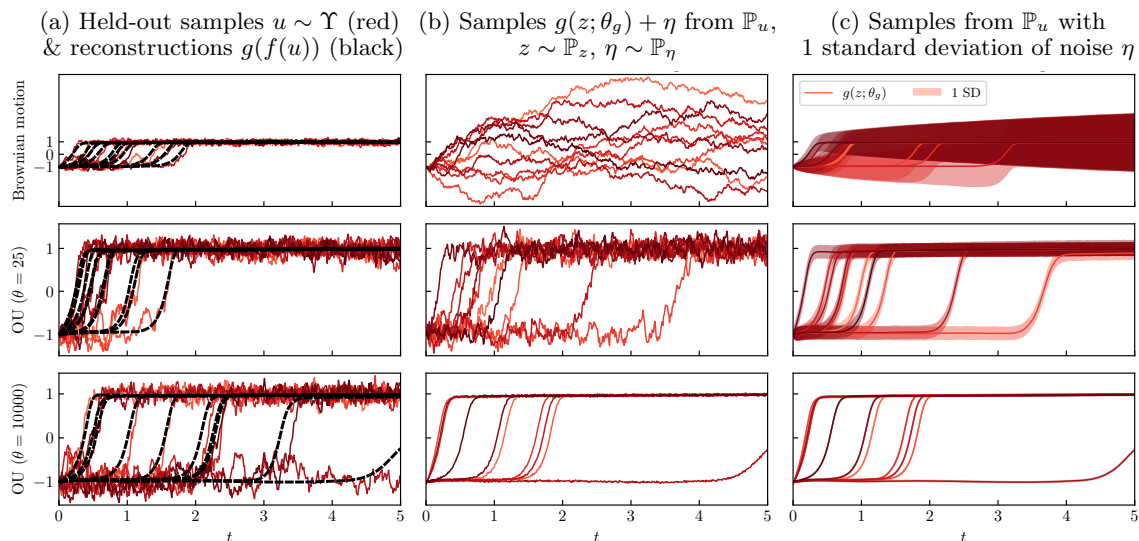


Figure 2.2: The SDE loss gives much freedom in the choice of decoder noise process  $\eta$ . The top row is governed by Brownian motion in the decoder and the second and third rows are governed, respectively, by two OU processes with different asymptotic variances. Taking Brownian motion as the noise process leads to high-quality reconstructions but a poor-quality generative model. Using a well-chosen OU process gives a much-improved generative model without perceptible degradation in reconstruction quality.

Using Brownian motion as the decoder noise (Figure 2.2), i.e.,  $c(x, t) = 0$  in (2.17), leads to excellent reconstructions, but samples from the generative model  $\mathbb{P}_u$ , i.e., realisations

$$u \mid z = g(z; \theta_g) + \eta, \quad z \sim \mathbb{P}_z, \quad \eta \sim \mathbb{P}_\eta \quad (2.26)$$

appear qualitatively different from the training data. By taking the law of an OU process as the reference measure, i.e., with  $c(x, t) = -\theta x$  for some  $\theta > 0$ , we obtain qualitatively similar reconstructions to those achieved under Brownian motion, but with samples that match the data distribution much more closely (Figure 2.2). This is because the variance of Brownian motion grows unboundedly with time, while the asymptotic variance under the OU process is  $\frac{\epsilon}{2\theta}$ , better reflecting the qualitative behaviour of the underlying data for suitably chosen  $\theta$ . In what follows, we use an OU process as the decoder noise with  $\theta = 25$ .

**Unsupervised learning of physically relevant quantities.** Our choice of latent dimension  $d_Z = 1$  was motivated by the heuristic that the time of the transition from  $x_1 = -1$  to  $x_2 = +1$  essentially determines the full SDE trajectory. FVAE identifies this variable purely from data: by taking equally spaced values of  $z \in [-2.5, 2.5]$  and examining the resulting functions  $g(z; \theta_g)$ , we see that larger values of  $z$  correspond to the transition occurring later in the time interval  $[0, T]$  (Figure 2.3(a)). While the values of  $z$  are equally spaced in  $[-2.5, 2.5]$ , the fact that more of the decoded paths transition in the time interval  $[0, 1]$  reflects the distribution of transition times in the underlying data.

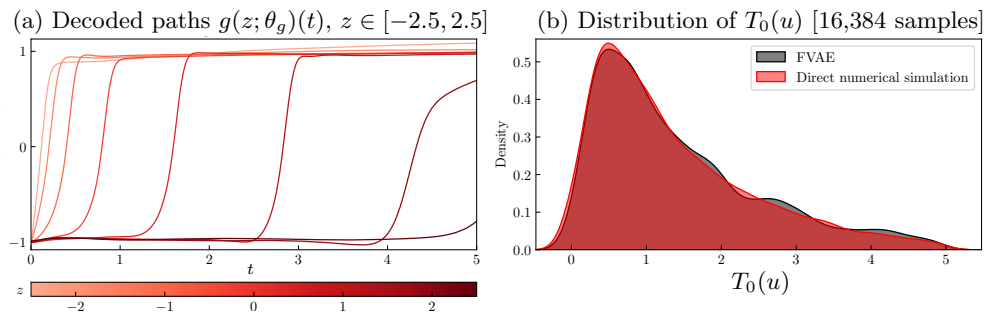


Figure 2.3: (a) The latent variable  $z$  identified by FVAE is in correspondence with the first-crossing time  $T_0$  of the decoded path  $g(z; \theta_g)$ . (b) Kernel density estimates of the distributions of  $T_0$  under the FVAE generative model and direct numerical simulations closely agree.

We also compare the distributions of the first-crossing time

$$T_0(u) = \inf\{t > 0 \mid u_t \geq 0\},$$

estimated using 16,384 paths from the generative model (2.26) and 16,384 direct numerical simulations of the SDE. We summarise these distributions using kernel density estimates with Gaussian kernels, selecting the bandwidths according to Scott's rule (Scott, 2015, eq. (6.44)). The two distributions closely agree (Figure 2.3(b)), showing that FVAE captures not only individual paths but also ensemble statistical properties of  $\Upsilon$ .

## 2.5.2 ESTIMATION OF MARKOV STATE MODELS

The evolution of molecules on long timescales is of significant interest in a variety of scientific applications. One example arises in the study of protein folding (Konovalov et al., 2021), where one wishes to capture the complex, multistage transitions of proteins between configurations. The high dimension of these systems means that numerical simulations are possible only on timescales orders of magnitudes shorter than those of physical interest.

Markov state models (MSMs) offer one method of distilling many short MD simulations into a statistical model permitting much longer simulations (see, e.g., Husic and Pande, 2018). Under the assumption that the underlying dynamics are given by a random process  $(u_t)_{t \geq 0}$  taking values in the configuration space  $X$ , MSMs partition the space into finitely many disjoint state sets,  $X = X_1 \cup \dots \cup X_p$ , and, for some **lag time**  $\tau > 0$ , consider the discrete-time process  $(U_k)_{k \in \mathbb{N}}$  defined such that  $U_k$  takes value  $i$  if  $u_{k\tau} \in X_i$ . When  $\tau$  is large enough that  $(U_k)_{k \in \mathbb{N}}$  is a Markov process, we can characterise the distribution of the process by estimating transition probabilities from the MD simulations; the resulting MSM can then be used to simulate on much longer timescales.

Motivated by this application, we show the power of FVAE in estimating transition probabilities using training data sampled at sparse or irregular intervals, where direct computation from the data may not be feasible. We illustrate this idea with an example based on the Brownian dynamics model (2.24) on the configuration space  $X = \mathbb{R}^2$  using a multiwell potential  $U$  (Figure 2.4(a)) given as the sum of a quadratic bowl perturbed a linear function and the negative of six Gaussian densities, with minima at  $(0, 0)$ ,  $(0.2, 0.2)$ ,  $(-0.2, -0.2)$ ,  $(0.2, -0.2)$ ,  $(0, 0.2)$  and  $(-0.2, 0)$ . We give the full expression for  $U$  in Appendix B.3.

Similarly to Section 2.5.1, we define the data space  $\mathcal{U} = C_0([0, T], X)$  and let  $\Upsilon \in \mathcal{P}(\mathcal{U})$  be the path measure associated with the SDE (2.24) with potential  $U$ , temperature  $\varepsilon = 0.1$ , final time  $T = 3$  and initial condition  $u_0 = 0$ . The training dataset consists of 16,384 sample paths provided at a timestep of  $3/512$ , where, for each sample, it is assumed that 50% of timesteps are missing from the training data in order to demonstrate FVAE’s ability to work with heterogeneous data. Data are generated using an Euler–Maruyama scheme as described in Appendix B.3. We train FVAE using the SDE loss (Section 2.3.1) using an OU process with  $\theta = 100$  as the decoder noise, zero-penalty scale  $\lambda = 50$ , regularisation scale  $\beta = 0.02$ , and latent dimension  $d_Z = 16$ .

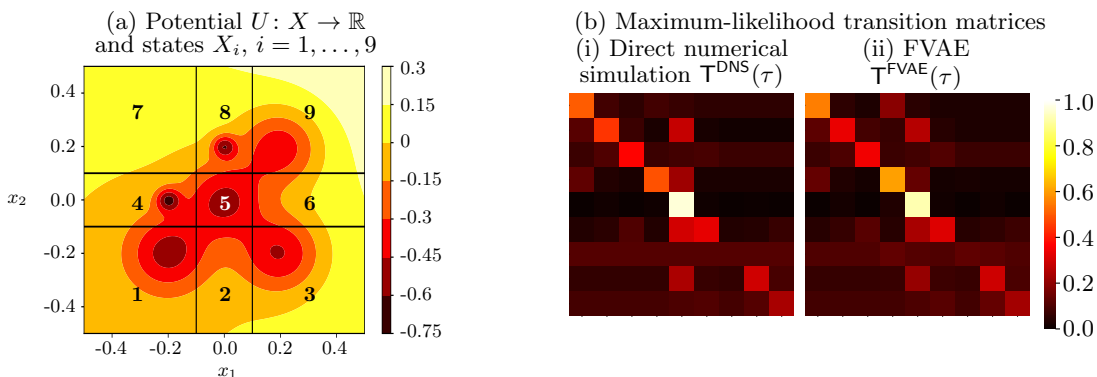


Figure 2.4: Transition matrices with lag time  $\tau = 3/512$  computed using FVAE compared to direct numerical simulation, both on the time interval  $[0, T]$ ,  $T = 3$ .

**Partitioning the configuration space  $X$ .** The states of a MSM can be selected manually using expert knowledge or automatically using variational or machine-learning methods (Mardt et al., 2018). For simplicity, we choose the states by hand, partitioning  $X = \mathbb{R}^2$  into  $p = 9$  disjoint regions (Figure 2.4(a)) divided by the four lines  $x_1 = \pm 0.1$  and  $x_2 = \pm 0.1$ .

**Using FVAE to estimate transition probabilities.** After training, FVAE can be used as a generative model to sample new trajectories similar to the training data, as already established in Section 2.5.1. Using FVAE allows us to generate these trajectories at any time discretisation, giving us significant flexibility in the choice of lag time  $\tau$ , even if the original training trajectories are discretised at irregular timesteps which differ from the desired lag time.

The lag time  $\tau$  has significant impact on the statistical properties of the resulting MSM (Nüske et al., 2017); while various methods exist to verify that the lag time is sufficiently large to ensure the process  $(U_k)_{k \in \mathbb{N}}$  is approximately Markov (see, e.g., Prinz et al., 2011, Sec. IV.F), for simplicity we focus on a fixed lag  $\tau = 3/512$  and set aside the question of Markovianity.

We draw  $N = 2,048$  trajectories  $(u^{(m)})_{m=1}^N$  from the FVAE generative model  $g(z) + \eta$ ,  $z \sim N(0, I_{d_z})$ ,  $\eta \sim \mathbb{P}_\eta$ , discretised on a mesh of  $K = 513$  points with timestep  $3/512$  on the time interval  $[0, T]$ . We then compute the count matrix

$$\mathbf{C}^{\text{FVAE}}(\tau) = (\mathbf{C}_{ij}^{\text{FVAE}}(\tau))_{i,j \in \{1, \dots, p\}}, \quad \mathbf{C}_{ij}^{\text{FVAE}}(\tau) = \sum_{k=0}^K \sum_{m=1}^N \mathbb{1} \left[ u_{k\tau}^{(m)} \in X_i \text{ and } u_{(k+1)\tau}^{(m)} \in X_j \right]$$

and derive the corresponding maximum-likelihood transition matrix  $\mathbf{T}^{\text{FVAE}}(\tau)$  by normalising each row of  $\mathbf{C}^{\text{FVAE}}(\tau)$  to sum to one; for simplicity we do not constrain the transition matrix to satisfy the detailed-balance condition (see Prinz et al., 2011, Sec. IV.D).

We compare the resulting transition matrix  $\mathbf{T}^{\text{FVAE}}(\tau)$  to the transition matrix  $\mathbf{T}^{\text{DNS}}(\tau)$  computed analogously using 2,048 direct numerical simulations on the regular timestep  $\tau$ , finding close agreement between the two transition matrices (Figure 2.4(b)).

### 3 Problems with VAEs in Infinite Dimensions

In Section 2.2, we derived a well-defined VAE objective in infinite dimensions under the assumption that  $\Upsilon \in \mathcal{P}(\mathcal{U} \parallel \mathbb{P}_\eta)$ , i.e.,

$$D_{\text{KL}}(\Upsilon \parallel \mathbb{P}_\eta) = \mathbb{E}_{u \sim \Upsilon} \left[ \log \frac{d\Upsilon}{d\mathbb{P}_\eta}(u) \right] < \infty. \quad (3.1)$$

This condition is also necessary in finite dimensions, but becomes increasingly significant—and difficult to satisfy—in infinite dimensions. In this section, we discuss the situations in which (3.1) fails, and the pathologies that arise when this is the case:

- (a) The ELBO  $\mathcal{L}(u; \theta_f, \theta_g)$  may be infinite for almost all  $u \in \mathcal{U}$ . This can result in the discretised training loss diverging as resolution is refined.
- (b) The ELBO  $\mathcal{L}(u; \theta_f, \theta_g)$  may be finite for each  $u \in \mathcal{U}$ , but its expectation over the data—the training objective  $\mathcal{J}(\theta_f, \theta_g)$ —may be infinite for all  $\theta_f \in \Theta_f$  and  $\theta_g \in \Theta_g$ . This manifests as a divergent training loss in the infinite-data limit.

- (c) The objective  $\mathcal{J}(\theta_f, \theta_g)$  may be infinite even when the population loss  $D_{\text{KL}}(\mathbb{Q}_{z,u}^{\theta_f} \parallel \mathbb{P}_{z,u}^{\theta_g})$  is finite, invalidating the probabilistic interpretation of FVAE.

Related issues arise quite broadly in statistical models with infinite-dimensional data. For nonparametric Bayesian methods, prior misspecification can lead to significant issues in interpreting the resulting posterior (see Ghosal and van der Vaart, 2017, Chapter 1.3). In the machine-learning literature, variational inference on function space arises in the context of Bayesian neural networks (Sun et al., 2019; Burt et al., 2021; Cinquin and Bamler, 2024), and the consequent issues are closely connected to those encountered in our study.

In Section 3.1, we describe the issues arising when  $d\Upsilon/d\mathbb{P}_\eta$  is undefined, and give a numerical example of a divergent training loss in the infinite-resolution limit as described in (a). In Section 3.2, we discuss the case that the density  $d\Upsilon/d\mathbb{P}_\eta$  exists but the finite-information condition (3.1) still fails, which can occur even in finite dimensions and leads to the situations described in (b) and (c).

### 3.1 Infinite ELBO

For the KL divergence  $D_{\text{KL}}(\Upsilon \parallel \mathbb{P}_\eta)$  to be finite, it is an essential prerequisite that  $\Upsilon \ll \mathbb{P}_\eta$ . In finite dimensions, this is almost always the case provided  $\mathbb{P}_\eta$  has full support; in infinite dimensions, however, absolute continuity is much more sensitive to small differences between measures, and a lack thereof is the “typical” behaviour even in relatively tame situations.

**Example 3.1 (No absolute continuity with Gaussian data and noise)** *Let  $\mathcal{U}$  be a separable Hilbert space, let  $\Upsilon = N(0, C)$  be a nondegenerate Gaussian measure with covariance operator  $C: \mathcal{U} \rightarrow \mathcal{U}$ , and let  $\mathbb{P}_\eta = N(0, \alpha C)$  for some  $\alpha > 0$ . Owing to the Feldman–Hájek dichotomy (see Bogachev, 1998, Ex. 2.7.4), even slight misspecification of  $\mathbb{P}_\eta$  leads to a failure of (3.1): the measures  $\Upsilon$  and  $\mathbb{P}_\eta$  are mutually singular unless  $\alpha = 1$ .*

Issues arising from a lack of absolute continuity are not purely theoretical, and can lead to the ELBO  $\mathcal{L}(u; \theta_f, \theta_g)$  being almost surely infinite, rendering training meaningless; in this case, discretisations of the continuum training objective will diverge as resolution is refined.

**Example 3.2 (Infinite ELBO when  $\Upsilon \perp \mathbb{P}_\eta$ )** *Consider the following generative model for (generalised) functions  $u$  defined on  $(0, 1)$ :*

$$\begin{aligned} \theta &\sim \text{Uniform}(0, 1), \\ u \mid \theta &= \delta_\theta, \end{aligned}$$

where  $\delta_x$  is a Dirac function centred at  $x \in (0, 1)$ . Since  $u$  almost surely takes values in the Sobolev space  $H^s((0, 1))$ ,  $s < -1/2$ , we take  $\mathcal{U} = H^{-1}((0, 1))$ , and let  $\Upsilon \in \mathcal{P}(\mathcal{U})$  denote the law of  $u$ . Suppose that  $\eta$  is white noise on  $L^2((0, 1))$ , so that  $\mathbb{P}_\eta \in \mathcal{P}(\mathcal{U})$  and  $H(\mathbb{P}_\eta) = L^2((0, 1))$ . The measures  $\Upsilon$  and  $\mathbb{P}_\eta$  are mutually singular, so (3.1) must fail; furthermore, the ELBO

$$\mathcal{L}(u; \theta_f, \theta_g) = \mathbb{E}_{z \sim \mathbb{Q}_{z|u}} \left[ \langle g(z; \theta_g), u \rangle_{L^2} - \frac{1}{2} \|g(z; \theta_g)\|_{L^2}^2 \right] - D_{\text{KL}}(\mathbb{Q}_{z|u} \parallel \mathbb{P}_z) \quad (3.2)$$

may be infinite or even undefined for each  $u \in \mathcal{U}$ , since the term  $\langle g(z; \theta_g), u \rangle_{L^2}$  is only defined up to  $\mathbb{P}_\eta$ -measure zero sets. This manner in which this problem manifests depends on the parametrisation of the decoder  $g$  and the discretisation of the terms in (3.2). We

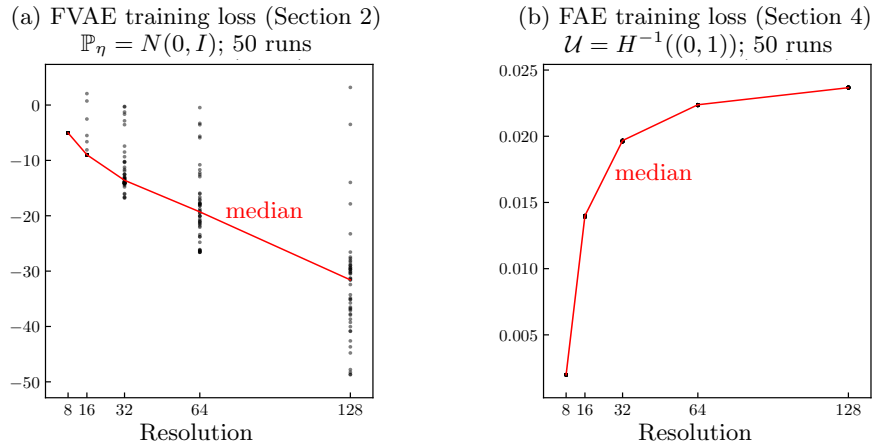


Figure 3.1: When the data measure  $\Upsilon$  is singular with respect to  $\mathbb{P}_\eta$ , the expectation of the ELBO (3.2) over the data measure is ill-defined, so the discretised training losses do not converge to a well-defined continuum limit. Further details in Appendix B.4. Using the FAE loss we shall propose in Section 4 leads to a well-defined continuum objective.

*demonstrate one possibility numerically (Figure 3.1) using a specially designed encoder and decoder architecture (Appendix B.4), finding that discretisations of the objective diverge to  $-\infty$  as the mesh is refined.*

The behaviour in the previous example can be ascribed to the misspecification of the decoder noise, and consequently of the FVAE generative model  $\mathbb{P}_u$ : realisations from  $\mathbb{P}_u$  are swamped in white noise and bear little resemblance to true samples from the data distribution. The previous example is also relevant in the analysis of VANO, with white decoder noise being the setting in which VANO works; we discuss this further in Section 5.

### 3.2 Lack of Correspondence Between Training Objective and Population Loss

Absolute continuity is necessary but not sufficient for (3.1) to hold: the expectation over  $u \sim \Upsilon$  may be infinite even if  $d\Upsilon/d\mathbb{P}_\eta(u)$  exists for all  $u \in \mathcal{U}$ . Such situations arise even in finite dimensions, and result in a divergence of the continuum training objective  $\mathcal{J}(\theta_f, \theta_g)$  in the infinite-data limit. Though this is of little concern in the typical machine-learning setup of a fixed training dataset, this issue is relevant in online learning and when fine-tuning an existing model on new data, since in this setting the dataset cannot be viewed as a finite collection. We give an example in  $\mathcal{U} = \mathbb{R}$ , and point out that our argument applies equally to the training objective corresponding to the usual ELBO of Kingma and Welling (2014).

**Example 3.3** *Let  $\mathcal{U} = \mathbb{R}$ , suppose that  $\Upsilon \in \mathcal{P}(\mathcal{U})$  is the law of a Cauchy distribution with median 0 and scale 1 and let  $\eta \sim N(0, \sigma^2)$  for some  $\sigma > 0$ . Even though  $\Upsilon \ll \mathbb{P}_\eta$ , the finite-information condition (3.1) fails since the Cauchy data distribution has far heavier tails than the Gaussian noise distribution. This leads to several undesirable behaviours.*



- (a) When  $\mathbb{Q}_{z|u} = \mathbb{P}_z$  for all  $u \in \mathcal{U}$  and  $g(z; \theta_g) = 1$  for all  $z \in \mathcal{Z}$ , the FVAE ELBO  $\mathcal{L}(u; \theta_f, \theta_g) = u - 1/2$  is clearly finite for each  $u \in \mathcal{U}$ . But, since all moments of the Cauchy distribution of order at least one are infinite, the training objective is infinite:

$$\mathcal{J}(\theta_f, \theta_g) = \mathbb{E}_{u \sim \Upsilon} [1/2 - u] = \infty.$$

Similar arguments apply to the VAE ELBO  $\mathcal{L}_{\text{VAE}}(u; \theta_f, \theta_g, \beta)$ . Moreover, examining the joint measures (2.6) and (2.8) reveals

$$\mathbb{P}_{z,u}(\mathrm{d}z, \mathrm{d}u) = \mathbb{P}_\eta(\mathrm{d}u - g(z; \theta_g))\mathbb{P}_z(\mathrm{d}z), \quad \mathbb{Q}_{z,u} = \Upsilon(\mathrm{d}u)\mathbb{P}_z(\mathrm{d}z),$$

and so  $D_{\text{KL}}(\mathbb{Q}_{z,u} \parallel \mathbb{P}_{z,u}) = D_{\text{KL}}(\Upsilon \parallel \mathbb{P}_\eta(\cdot - 1)) = \infty$ .

- (b) Let  $h: \mathbb{R} \rightarrow \mathbb{R}$  be an increasing map such that if  $z \sim \mathbb{P}_z$ , then  $h(z) \sim \Upsilon$ , derived, for example, through the inverse transform method. When  $\mathbb{Q}_{z|u} = \mathbb{P}_{z|u}$  for all  $u \in \mathcal{U}$  and  $g(z; \theta_g) = h(z)$ , we conclude that  $\mathbb{P}_u = \Upsilon * \mathbb{P}_\eta$  and the joint measures (2.7) and (2.8) factorise as

$$\mathbb{P}_{z,u}(\mathrm{d}z, \mathrm{d}u) = (\Upsilon * \mathbb{P}_\eta)(\mathrm{d}u)\mathbb{P}_{z|u}(\mathrm{d}z), \quad \mathbb{Q}_{z,u}(\mathrm{d}z, \mathrm{d}u) = \Upsilon(\mathrm{d}u)\mathbb{P}_{z|u}(\mathrm{d}z),$$

so  $D_{\text{KL}}(\mathbb{Q}_{z,u} \parallel \mathbb{P}_{z,u}) = D_{\text{KL}}(\Upsilon \parallel \Upsilon * \mathbb{P}_\eta) < \infty$ . But, as a consequence of (2.11), since  $D_{\text{KL}}(\Upsilon \parallel \mathbb{P}_\eta) = \infty$ , the training objective  $\mathcal{J}(\theta_f, \theta_g)$  must also be infinite.

Consequently, when (3.1) fails, the correspondence between minimising the population loss  $D_{\text{KL}}(\mathbb{Q}_{z,u}^{\theta_f} \parallel \mathbb{P}_{z,u}^{\theta_g})$  and the training objective  $\mathcal{J}(\theta_f, \theta_g)$  is broken.

## 4 Regularised Autoencoders on Function Space

Unless a suitable choice of decoder noise  $\mathbb{P}_\eta$  exists with so that the finite-information condition  $\Upsilon \in \mathcal{P}(\mathcal{U} \parallel \mathbb{P}_\eta)$  holds, the FVAE objective may be ill-defined and the training objective infinite. This is a significant obstacle in infinite dimensions: for many data distributions, it may be difficult—or even impossible—to find an appropriate choice of  $\mathbb{P}_\eta$ . To overcome this, we set aside the probabilistic motivation for VAEs and define a regularised autoencoder in function space—which we call the **functional autoencoder (FAE)**—that avoids the need for onerous conditions on the data measure.

In Section 4.1, we state this objective and point out connections to the FVAE objective. In Section 4.2, we outline minor adaptations to the FVAE encoder and decoder to the regularised autoencoder framework. In Section 4.3, we demonstrate our proposed method, FAE, on two examples from scientific machine learning.

### 4.1 Objective and Algorithms

Let  $\mathcal{U}$  be a separable Banach space, let  $\mathcal{Z} = \mathbb{R}^{d_z}$ , and assume  $\Upsilon \in \mathcal{P}(\mathcal{U})$ . Define a parametrised class of **encoders**  $f: \mathcal{U} \times \Theta_f \rightarrow \mathcal{Z}$  and a class of **decoders**  $g: \mathcal{Z} \times \Theta_g \rightarrow \mathcal{U}$ , where, unlike in Section 2,  $f$  now returns a single latent vector  $f(u; \theta_f) \in \mathcal{Z}$  and  $g$  is no longer constrained to take values in a subspace  $\mathcal{V} \subset \mathcal{U}$ .

We define a regularised autoencoder as the sum of a misfit term on the data space  $\mathcal{U}$  and a regularisation term on the latent space  $\mathcal{Z}$  with **regularisation scale**  $\beta > 0$ :

$$\mathcal{J}_{\text{FAE}}(u; \theta_f, \theta_g, \beta) = \mathbb{E}_{u \sim \Upsilon} \left[ \frac{1}{2} \|g(f(u; \theta_f); \theta_g) - u\|_{\mathcal{U}}^2 + \beta \|f(u)\|_2^2 \right]. \quad (4.1)$$

There is great flexibility in the choice of regularisation term; we adopt the Euclidean norm as a simplifying choice consistent with using a Gaussian prior in FVAE (Remark 2.5). While (4.1) has much in common with the FVAE objective  $\mathcal{J}(\theta_f, \theta_g)$ , it is not marred by the foundational issues raised by our analysis in Section 3; indeed, the FAE objective is very broadly applicable thanks to the following result, proven in Appendix A.2.

**Proposition 4.1** *Let  $\mathcal{U}$  be a separable Banach space. Suppose that  $\Upsilon \in \mathcal{P}(\mathcal{U})$  has finite second moment, i.e.,  $\mathbb{E}[\|u\|_{\mathcal{U}}^2] < \infty$ . Then, provided that there exists  $\theta_f \in \Theta_f$  and  $\theta_g \in \Theta_g$  such that  $f(u; \theta_f) = 0$  and  $g(z; \theta_g) = 0$ , the infimum of (4.1) is finite.*

In the numerical examples of Section 4.3, we take  $\mathcal{U} = L^2(\Omega)$ , where  $\Omega = \mathbb{T}^d$  or  $\Omega = [0, 1]^d$ . We then discretise the  $\mathcal{U}$ -norm, on a given mesh  $\{x_i\}_{i=1}^n$ , with the sum

$$\|u\|_{L^2(\Omega)}^2 \approx \frac{1}{n} \sum_{i=1}^n \|u(x_i)\|_2^2, \quad u \in \mathcal{U}.$$

**Remark 4.2** *We emphasise that our framework can be applied whenever  $\mathcal{U}$  is Banach. One can readily imagine, for example, taking  $\mathcal{U}$  to be a Sobolev space of order  $s \geq 1$  when derivative information is known for the data (Czarnecki et al., 2017), and approximating the  $L^2$  norm of the data and its derivative by sums. More generally we may use characterising linear functionals on the Banach space as the starting point for approximation.*

## 4.2 Architecture and Training

We propose a slight modification of the FVAE architecture proposed in Section 2.4 for use with our regularised autoencoding framework. The only practical change is in the encoder, which no longer computes parameters for a variational distribution; instead, we parametrise the encoder  $f: \mathcal{U} \times \Theta_f \rightarrow \mathcal{Z}$  directly as a function-to-vector map as in (2.22), with range  $\mathbb{R}^{dz}$ . All other architectural details remain unchanged from Section 2.4, and in particular we shall frequently make use of the self-supervised training scheme described in Section 2.4.4.

To complement this mesh-invariant architecture, we now propose a self-supervised training scheme that appears to be new to the operator-learning literature; the practical benefits of this scheme will be demonstrated in Section 4.3.

## 4.3 Numerical Examples

In Sections 4.3.1 and 4.3.2, we apply FAE as an out-of-the-box method to discover a low-dimensional latent space for solutions to the incompressible Navier–Stokes equations and the Darcy model for flow in a porous medium, respectively. We find that:

- (a) FAE’s mesh-invariant architecture autoencodes with performance broadly comparable to convolutional neural network (CNN) architectures of comparable size (Section 4.3.1).

- (b) The ability to discretise the encoder and decoder on different meshes enables new applications to inpainting and data-driven superresolution (Section 4.3.1), as well as extensions of existing zero-shot superresolution as proposed by VANO (Section 4.3.2).
- (c) Self-supervised training significantly improves performance under mesh changes (Section 4.3.1) and can accelerate training while reducing memory demand (Section 4.3.2).
- (d) Training a generative model on the FAE latent space leads to a resolution-invariant generative model which accurately captures distributional properties (Section 4.3.2).

#### 4.3.1 NAVIER–STOKES EQUATIONS

We first illustrate how FAE can be used to learn a low-dimensional representation for snapshots of the vorticity of a fluid flow in two spatial dimensions governed by the Navier–Stokes equations, and illustrate some of the benefits of our resolution-invariant framework.

Let  $\Omega = \mathbb{T}^2$  be the periodic torus, viewed as the square  $[0, 1]^2$  with opposing edges identified and unit normal  $\hat{z}$ , and let  $\mathcal{U} = L^2(\Omega)$ . While the Navier–Stokes equations are typically formulated in terms of the primitive variables of velocity  $u$  and pressure  $p$ , it is more natural in this case to work with the vorticity–streamfunction formulation (see, e.g., Chandler and Kerswell, 2013, eq. (2.6)). In particular the vorticity  $\nabla \times u$  is zero except in the out-of-plane component  $\hat{z}\omega$ . The scalar component of the vorticity,  $\omega$ , then satisfies

$$\begin{aligned} \partial_t \omega &= \hat{z} \cdot (\nabla \times (u \times \omega \hat{z})) + \nu \Delta \omega + \varphi && \text{on } \Omega \times (0, T], \\ \omega(x, 0) &= \omega_0(x) && \text{on } \Omega. \end{aligned} \tag{4.2}$$

In this formulation the velocity  $u = \nabla \times (\psi \hat{z})$  where the streamfunction  $\psi$  satisfies  $\omega = \Delta \psi$ . Thus  $\psi$  is uniquely defined, up to an irrelevant constant, in terms of  $\omega$ , and (4.2) defines a closed evolution equation for  $\omega$ .

We suppose that  $\Upsilon \in \mathcal{P}(\mathcal{U})$  is the distribution of the scalar vorticity  $\omega(\cdot, T)$  at  $T = 50$  given by (4.2), with viscosity  $\nu = 10^{-4}$ , and forcing

$$\varphi(x) := \frac{1}{10} \left( \sin(2\pi(x_1 + x_2)) + \cos(2\pi(x_1 + x_2)) \right).$$

We assume that the initial condition  $\omega_0$  has distribution  $N(0, C)$  with covariance operator  $C = 7^{3/2}(49I - \Delta)^{-5/2}$ , where  $\Delta$  is the Laplacian operator for spatially-mean-zero functions on the torus  $\mathbb{T}^2$ . The training dataset, based on that of Li et al. (2021), consists of 8,000 samples from  $\Upsilon$  generated on a  $64 \times 64$  grid using a pseudospectral solver, and a further 2,000 independent samples are held out as an evaluation set; the data are scaled so that  $\omega(x, T) \in [0, 1]$  for all  $x \in \Omega$ . Further details are provided in Appendix B.5.

We train FAE with latent dimension  $d_{\mathcal{Z}} = 64$  and regularisation scale  $\beta = 10^{-3}$ , and use self-supervised training (Section 2.4.4), masking 70% of input mesh points and evaluating the decoder on the masked mesh points. Throughout, given a mesh  $\{x_i\}_{i=1}^n$ , we evaluate autoencoding performance through the MSE in  $\mathcal{U}$  averaged over the held-out data  $(u^{(k)})_{k=1}^N$ :

$$\text{MSE}(\theta_f, \theta_g)^2 \approx \frac{1}{nN} \sum_{k=1}^N \sum_{i=1}^n \left( g(f(u^{(k)}; \theta_f); \theta_g)(x_i) - u^{(k)}(x_i) \right)^2. \tag{4.3}$$

**Performance at fixed resolution.** We compare the autoencoding performance of our mesh-invariant FAE architecture to a fixed-resolution CNN used “off the shelf”, both trained using the FAE objective with all other hyperparameters the same. Our goal is to understand whether our architecture is competitive even without the inductive bias of CNNs.

We train one instance of FAE with each architecture on data discretised on a  $64 \times 64$  grid, without masking (details in Appendix B.5). When autoencoding held-out data from the evaluation set, we find that our FAE architecture achieves MSE only slightly larger than the CNN architecture, with a comparable number of parameters (Figure 4.1). It is reasonable to expect some tradeoff between fixed-resolution performance and the ability to change meshes; further research is desirable to close this gap through better mesh-invariant architectures.

Autoencoding on evaluation set ( $64 \times 64$ grid)		
	MSE (4.3)	Parameters
FAE architecture	$4.81 \times 10^{-4}$ $\pm 0.17 \times 10^{-4}$	64,857
CNN architecture	$2.32 \times 10^{-4}$ $\pm 0.05 \times 10^{-4}$	71,553

Mean  $\pm$  1 standard deviation; 5 training runs  
Figure 4.1: Our resolution-invariant architecture performs comparably to off-the-shelf CNN architectures at similar parameter counts.

**Inpainting.** FAE can encode and decode on different meshes, making it a natural tool for inpainting—inferring missing parts of the input function based on the observed data and knowledge of the underlying data distribution acquired through training. Methods to solve inpainting and related inverse problems are actively researched across the computer-vision community; see, e.g., Quan et al. (2024). Owing to the mesh-invariance of our architecture, our proposed FAE can solve a variety of inpainting tasks with a single trained model.

We evaluate the inpainting performance of FAE—trained as described at the start of the section—by taking data drawn from the evaluation set, discretised on a  $64 \times 64$  grid, and applying a variety of masks:

- (i) masking of 95% of mesh points, randomly selected;
- (ii) masking of a square with random centre and random side length; and
- (iii) masking of a  $-0.05$ -superlevel set of a Gaussian random field  $N(0, (\tau^2 I - \Delta)^{-d})$ , where  $\Delta$  is the Laplacian on the torus and  $\tau = 30$  and  $d = 1.2$ .

We encode each masked sample and decode on a  $64 \times 64$  grid (Figure 4.2), finding that reconstructions agree with the ground truth and FAE proves robust even to significant levels of masking. As a consequence of the autoencoding procedure, the unmasked region of the input may also be modified, an effect that is most pronounced in (ii), where some features in the input are lost in the reconstruction. We hypothesise that the failure to capture fine-scale features could be mitigated with more sophisticated neural-operator architectures that better capture the very fine-scale features; we leave this to future work.

The percentage of mesh points masked during self-supervised training has a significant influence on inpainting quality; to quantify the tradeoffs, we train instances of FAE with masking, preserving a **point ratio** of 10%, 50% and 90% of the input mesh points during training, respectively, holding all other hyperparameters constant. We evaluate each model by encoding held-out data with a given point ratio and computing the reconstruction MSE (4.3) on a  $64 \times 64$  grid (Figure 4.2(b)). We find that models trained with the encoder discretised on a low point ratio perform better when evaluated on data with a high point

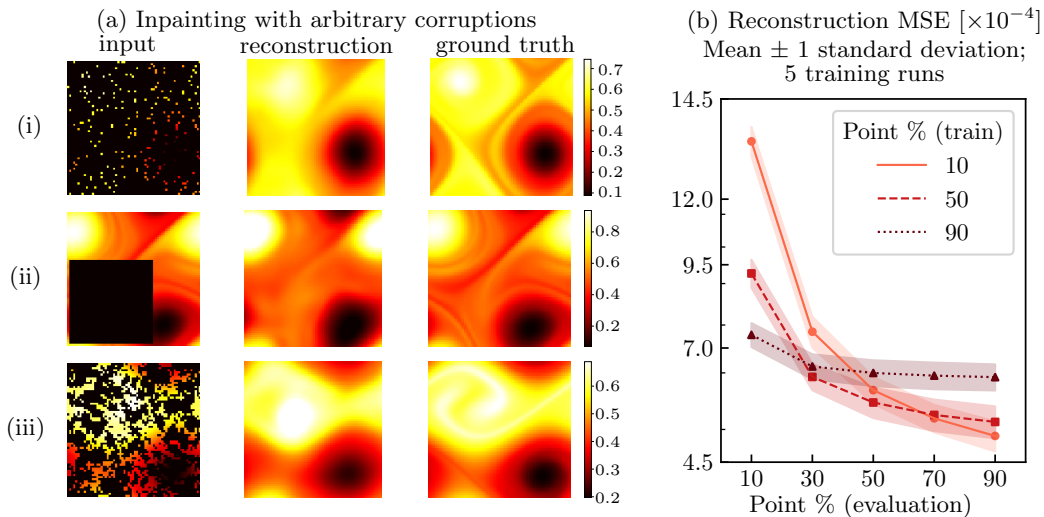


Figure 4.2: (a) By encoding inputs on a given mesh and decoding on a grid, FAE can solve a variety of inpainting tasks. Further samples are provided in Appendix B.5. (b) Training the encoder on a sparse mesh has a regularising effect on FAE, leading to lower evaluation MSE on dense meshes, but harms performance when evaluating on very sparse meshes.

ratio, which we hypothesise is due to the regularising effect of training with few mesh points. On the other hand, such models perform poorly on sparsely sampled evaluation data with a low point ratio, likely because when training on sparse meshes the encoder is very unlikely to have seen a mesh that coincides with the mesh seen at evaluation time. We conclude that training with relatively low levels of masking (e.g., 90% of points unmasked) is best when the goal is to evaluate on very sparse data, but this incurs a moderate cost when the evaluation mesh is dense. Further analysis on this tradeoff is provided in Appendix B.5.

While we do not consider it here, the random masking applied during self-supervised training could be further augmented with other types of masks, such as polygons, with the aim of improving the robustness of FAE to similar masks at evaluation time.

**Superresolution.** The ability to encode and decode on different meshes also makes FAE a flexible method for (single-image) superresolution: reconstruction of a high-resolution output from a single low-resolution input (see Li et al., 2024). Deep-learning-based superresolution methods have also found use in fluid dynamics, e.g., in increasing the resolution (“downscaling”) of numerical simulations (Kochkov et al., 2021; Bischoff and Deck, 2024). An advantage of FAE over many other approaches is that a single trained model can be applied to any input resolution and upsampling factor.

We first evaluate the performance of FAE for **data-driven superresolution**, where the model is trained at high resolution and used to enhance lower-resolution inputs. After training, we encode inputs at resolution  $8 \times 8$  and  $16 \times 16$  and decode on the original  $64 \times 64$  training resolution (Figure 4.3(a)). FAE is able to resolve features not visible in the inputs using structure learned from the training data, and, while reconstruction MSE grows as the input resolution is decreased (Figure 4.3(b)), the perceptual quality remains good even at resolution  $8 \times 8$ . As with inpainting, superresolution performance could be further improved with an architecture that is better able to capture the turbulent dynamics in the data.

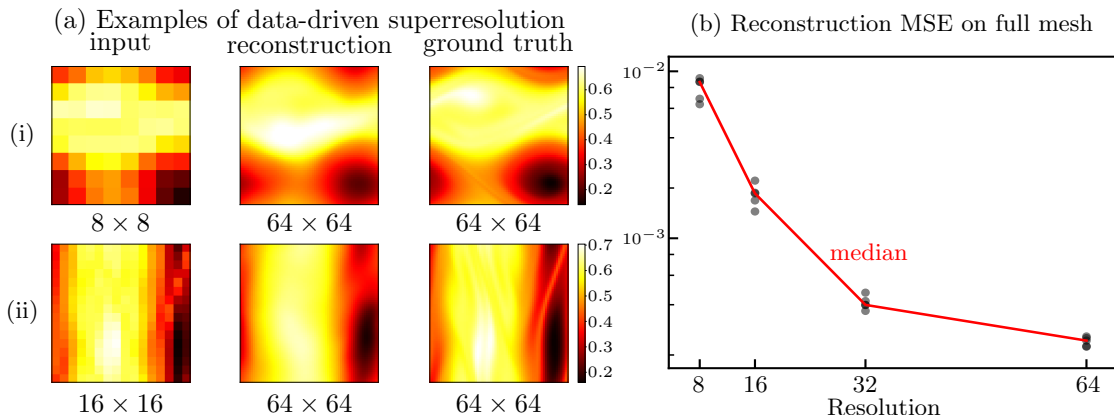


Figure 4.3: (a) FAE is able to encode inputs on low-resolution grids and decode at higher resolution, recovering fine-scale features using knowledge of the underlying data distribution. Further uncurated samples are provided in Appendix B.5. (b) Superresolution becomes increasingly difficult as the resolution of the input decreases, but FAE performs well even with very low resolution inputs.

We also investigate the stability of FAE for **zero-shot superresolution** (see, e.g., Li et al., 2021), where the model is evaluated on higher resolutions than seen during training. Our architecture proves robust when autoencoding on meshes much finer than the original  $64 \times 64$  training grid (Figure 4.4(a)). As in our discussion of inpainting, the main limitation is the underlying representation capacity of the architecture, which results in the loss of some fine-scale features present even in the  $64 \times 64$  input. Thanks to the coordinate MLP architecture of our decoder, we can decode on extremely fine meshes without exhausting the GPU memory (details in Appendix B.5). We point out that zero-shot superresolution is only possible with VANO when the input is given on the same mesh seen during training; FAE does not have this constraint.

In our investigation of zero-shot superresolution, we do not embed prior information or train FAE above resolution  $64 \times 64$ , so we do not expect to resolve high-frequency features beyond those seen during training. Nevertheless, the robustness to mesh changes we observe validates the approximate resolution-invariance of our architecture.

**Applications of the latent space  $\mathcal{Z}$ .** The regularised FAE latent space gives a well-structured finite representation of the infinite-dimensional data  $u \in \mathcal{U}$ , extracting the intrinsic features of the data in a resolution-invariant way. We expect there to be benefit in using this latent representation as a building block for applications such as supervised learning and generative modelling on functional data, and draw parallels with the many other operator-learning methods with encoder–decoder structure (Seidman et al., 2022).

To verify that the latent space is indeed well-structured, we draw samples  $u_1$  and  $u_2$  from the evaluation set, compute the latents  $z_1 = m(u_1)$  and  $z_2 = m(u_2) \in \mathcal{Z}$ , and evaluate the decoder  $g$  along the convex combination  $z_1\alpha + z_2(1-\alpha)$ . This leads to a sensible interpolation in  $\mathcal{U}$ , indicating that the latent space has been effectively regularised (Figure 4.4(b)).

**Efficient superresolution on regions of interest.** Since the FAE decoder can be evaluated on any mesh, we can perform superresolution in a specific region of interest without

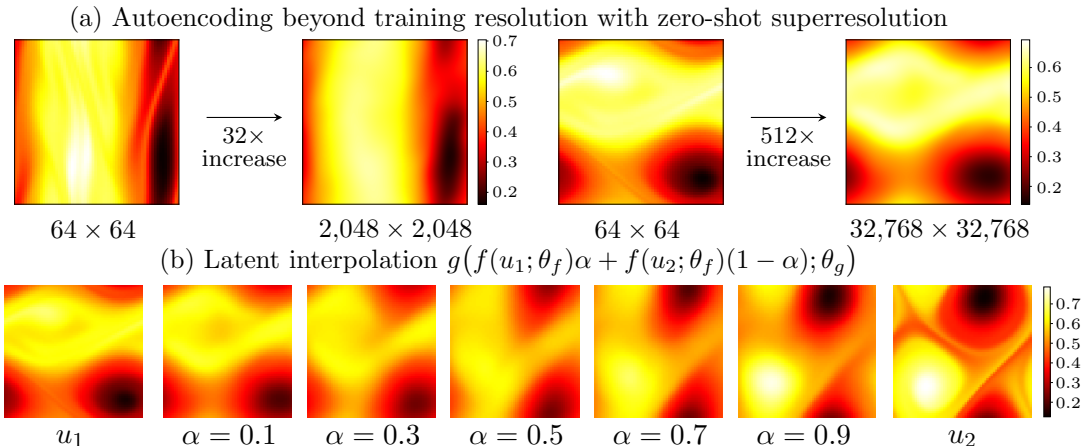


Figure 4.4: (a) FAE can stably decode at resolutions much higher than the training resolution (best viewed digitally). (b) The regularised latent space  $\mathcal{Z}$  allows for meaningful interpolation between samples. Further examples are given in Appendix B.5.

the need to upsample across the whole domain. This could also be done adaptively, decoding first on a coarse grid and then refining on a specific region to resolve finer details on demand. Doing this leads to significant savings through reduced inference time, memory usage, and energy cost. We note that similar strategies could also be possible with VANO.

To illustrate the potential savings, we consider the task of decoding on a circular subregion of interest with target mesh spacing  $1/400$  (Figure 4.5(a)). Achieving this resolution over the whole domain—corresponding to a  $400 \times 400$  grid—would involve 160,000 evaluations of the decoder network; decoding on the subregion requires just  $1/4$  of this (Figure 4.5(b)).

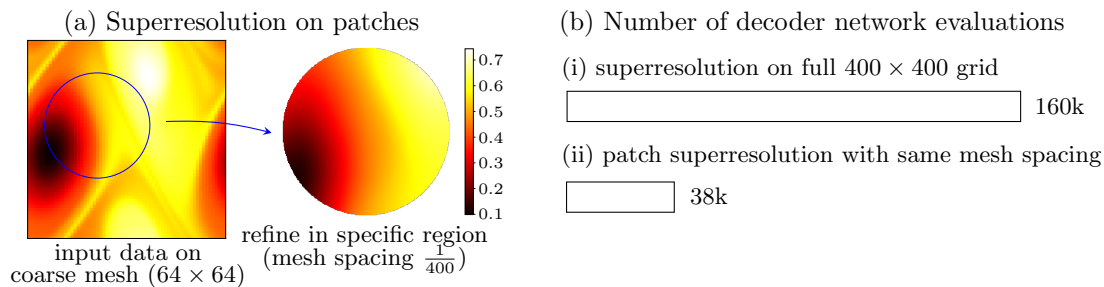


Figure 4.5: The FAE decoder can be discretised on arbitrary meshes, allowing for efficient superresolution on regions of interest (best viewed digitally).

### 4.3.2 DARCY FLOW

Darcy flow is a model of steady-state flow in a porous medium, derivable from first principles using homogenisation; see, e.g., Freeze and Cherry (1979, Sec. 2.11) and Keller (1980). We restrict attention to the two-dimensional domain  $\Omega = [0, 1]^2$  and suppose that, for some permeability field  $k: \Omega \rightarrow \mathbb{R}$  and forcing  $\varphi: \Omega \rightarrow \mathbb{R}$ , the pressure field  $p: \Omega \rightarrow \mathbb{R}$  satisfies

$$\begin{aligned} -\nabla \cdot (k\nabla p) &= \varphi && \text{on } \Omega, \\ p &= 0 && \text{on } \partial\Omega. \end{aligned} \tag{4.4}$$

We assume  $\varphi := 1$  and that  $k \sim \mu$  is distributed as the pushforward of the measure  $N(0, (-\Delta + 9I)^{-2})$ , where  $\Delta$  is the Neumann Laplacian, under the map  $\psi(x) := 3 + 9 \cdot \mathbf{1}[x \geq 0]$ . We take  $\mathcal{U} = L^2(\Omega)$  and define the data measure  $\Upsilon \in \mathcal{P}(\mathcal{U})$  to be the pushforward of  $\mu$  under the solution operator  $\mathcal{G}: k \mapsto p$  to the system (4.4). While solutions to the elliptic PDE (4.4) can be expected to have much greater than  $L^2$ -regularity (see, e.g., Evans, 2010, Sec. 6.3), we assume only that  $p \in L^2(\Omega)$  to show the versatility of our method.

The training dataset is based on that of Li et al. (2021) and consists of 1,024 samples from  $\Upsilon$  discretised on a  $421 \times 421$  grid, generated using a finite-difference method, with a further 1,024 samples generated in the same manner held out as an evaluation set. Data are scaled so that  $p(x) \in [0, 1]$  for all  $x \in \Omega$ , and we provide further details of the training data in Appendix B.6. We train FAE with latent dimension  $d_{\mathcal{Z}} = 64$ , regularisation scale  $\beta = 10^{-3}$ , and use self-supervised training, masking 70% of input mesh points and decoding on unseen mesh points. Where specified, we downsample training and evaluation data as described in Appendix B.6, and, as in (4.3), autoencoding is evaluated with a discretisation of the MSE in  $\mathcal{U}$ .

**Accelerating training using self-supervised learning.** As well as improving reconstruction quality and robustness to mesh changes, self-supervised training can significantly reduce the time and memory cost of training. As evaluation cost scales linearly with the number of mesh points, masking a high proportion of mesh points in both the encoder and decoder significantly reduces GPU demand.

To illustrate the numerical benefits, we compare the training dynamics over time for FAE trained on the data downsampled to resolution  $211 \times 211$  with the encoder and decoder discretised with the same point ratio on distinct random meshes to maximise computational savings. Both models are trained on a single NVIDIA GeForce RTX 4090 with 24GB of VRAM with batch size 32, stopping once reconstruction MSE on a held-out set plateaus. We evaluate both models through MSE on evaluation data discretised on a  $211 \times 211$  grid.

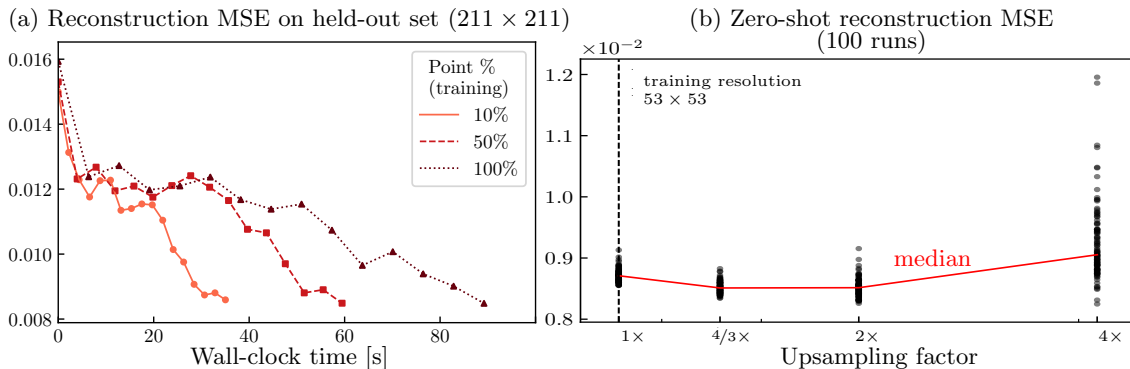


Figure 4.6: (a) For high-resolution data, training with masking in the encoder and decoder reduces computational cost and allows for better resource use, leading to significantly faster convergence. (b) On the Darcy flow dataset, FAE’s zero-shot reconstruction MSE compared to high-resolution ground truth remains low even at  $4\times$  training resolution.

The models trained with masking converge significantly faster as the smaller data tensors allow for better use of the GPU parallelism (Figure 4.6(a)). At higher resolutions, memory



constraints may entirely preclude training on the full grid, while training with masking enables training at much higher resolutions without exhausting GPU memory.

Related ideas have been used in the adaptive-subsampling training scheme for FNOs proposed by Lanthaler et al. (2024), which involves training first on a coarse grid and refining the mesh each time a given evaluation metric plateaus. Our approach differs by dropping mesh points randomly, which would not be possible with the grid-based FNO. One can readily imagine training FAE with a combination of adaptive subsampling and self-supervised learning; we leave this to future work.

**Zero-shot superresolution.** We evaluate the performance of FAE’s zero-shot superresolution quantitatively using the high-resolution ground truth available in this dataset. After training FAE on data downsampled to resolution  $53 \times 53$ , we evaluate FAE on held-out data, discretising the encoder on a  $53 \times 53$  grid and discretising the decoder on a finer mesh. We find that, on this dataset, upsampling by factors  $4/3$  and  $2$  possibly leads to slightly reduced MSE, which we expect is a result of minor artifacts caused by the downsampling procedure during training, while upsampling by a factor of  $4$  leads to modestly increased MSE (Figure 4.6(b)). These results suggest that FAE is robust at resolutions far above those seen during training, and does not suffer from severe degeneration when changing resolution.

We emphasise that the smooth pressure fields in this dataset (see Figure 4.7(a)) mean there is little high-frequency content beyond that seen during training, so it is not surprising that the error is relatively stable at higher resolutions; our intention is not to extrapolate but to verify stability of our architecture under mesh changes. For the turbulent flows in Section 4.3.1, we expect that the error would significantly increase at higher resolutions owing to the fine-scale features unseen during training.

**Generative modelling.** Unlike FVAE, our proposed FAE is not inherently a generative model. Instead, we can construct a generative model on the regularised autoencoder latent space (see Ghosh et al., 2020; Vahdat et al., 2021), resulting in a resolution-invariant generative model. More precisely, by learning the distribution  $\Lambda \in \mathcal{P}(\mathcal{Z})$  of  $z$  given by

$$z \mid u = f(u; \theta_f), \quad u \sim \Upsilon \tag{4.5}$$

with a fixed-resolution generative model  $\mathbb{P}_z \in \mathcal{P}(\mathcal{Z})$ , it is then straightforward to sample from the FAE generative model  $\mathbb{P}_u \in \mathcal{P}(\mathcal{U})$  for  $u$  given by

$$u \mid z = g(z; \theta_g), \quad z \sim \mathbb{P}_z. \tag{4.6}$$

Provided  $\Lambda \approx \mathbb{P}_z$  and  $g(f(u)) \approx u$  for  $u \sim \Upsilon$ , samples from  $\mathbb{P}_u$  will be approximately distributed according to  $\Upsilon$ . Unlike many other generative models on function space (which we survey in Section 5), our approach pushes forward a finite-dimensional latent variable that can be sampled at low cost; thanks to our mesh-invariant architecture, this can be decoded on any mesh and refined on demand, similar to the experiments in Section 4.3.1.

As a simple illustration of the idea, we take FAE, trained at resolution  $47 \times 47$  with self-supervised training as described at the start of the section, and seek to extend this with a generative model. We fit a Gaussian mixture model  $\mathbb{P}_z$  with 10 components to the distribution  $\Lambda$  described in (4.5) using the expectation-maximisation algorithm (see Bishop, 2006, Section 9.2.2). Samples from the generative model  $\mathbb{P}_u$  closely resemble samples from the underlying data measure  $\Upsilon$  (Figure 4.7(a)).

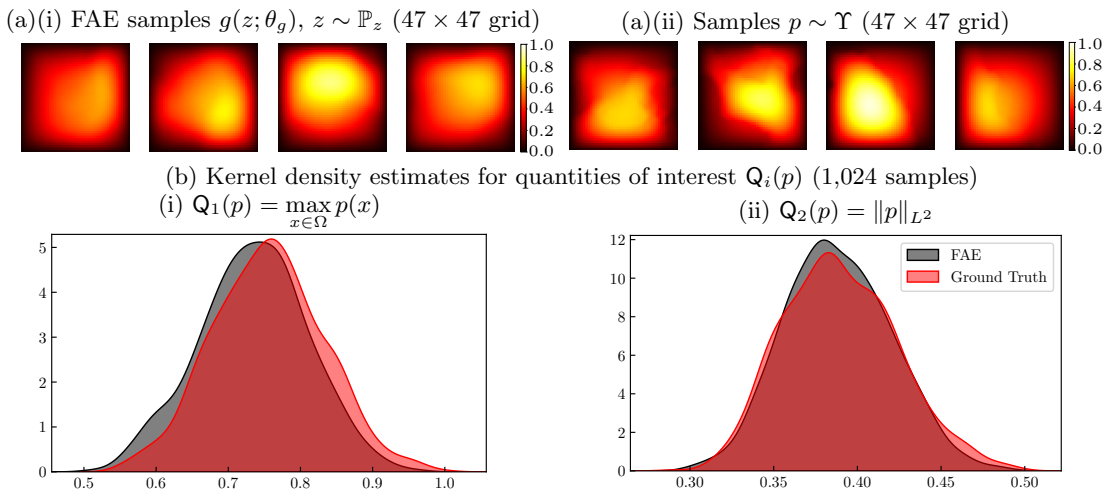


Figure 4.7: (a) Uncurated samples from the FAE generative model for the pressure field  $p$ . Further samples are provided in Appendix B.6. (b) The distributions of quantities of interest computed using the FAE generative model closely agree with the ground truth.

To measure generative performance, we approximate the distributions of physically relevant quantities of interest  $Q_i(p)$  depending on the data  $p \in \mathcal{U}$  using 1,024 samples generated from  $\mathbb{P}_u$  and  $\Upsilon$ . Following the procedure used in Figure 2.3(b) to generate kernel density estimates, we see close agreement between the distributions (Figure 4.7(b)). While it would also be possible to evaluate the generative model using statistical distances such as maximum mean discrepancy (Borgwardt et al., 2006), we focus on comparisons using more easily interpretable quantities relevant to the physical system at hand.

Though we adopt the convention of training the autoencoder and generative model separately (Rombach et al., 2022) here, the models could also be trained jointly; we leave this, and an investigation of generative models on the FAE latent space, to future work.

## 5 Related Work

**Variational autoencoding neural operators.** The VANO model (Seidman et al., 2023) also extends the VAE objective to function space and uses ideas from operator learning to construct a model that can decode at any resolution. Our approach differs substantially in both the training objective and in practical implementation, as we outline below.

The most significant difference is in the formulation of the underlying loss on function space. The VANO loss is derived using the same generative model (2.5) as our work, restricted to the case that the decoder noise  $\eta$  is white noise on  $L^2(\Omega)$ , with  $\Omega = [0, 1]^d$ , i.e.,  $\mathbb{P}_\eta = N(0, I)$ ; under these assumptions,  $\eta$  takes values in  $\mathcal{U} = H^{-s}(\Omega)$ ,  $s < -d/2$ . Unlike our approach, VANO’s loss (Seidman et al., 2023, Theorem 4.1) is formulated as an extension of the ELBO (2.4), which, in our notation takes the form

$$\begin{aligned} \mathcal{L}_{\text{VANO}}(u; \theta_f, \theta_g, \beta) &= \mathbb{E}_{z \sim \mathbb{Q}_{z|u}} \left[ -\log \frac{d\mathbb{P}_{u|z}}{d\mathbb{P}_\eta}(u; \theta_g) \right] + \beta D_{\text{KL}}(\mathbb{Q}_{z|u}^{\theta_f} \| \mathbb{P}_z) \\ &= \mathbb{E}_{z \sim \mathbb{Q}_{z|u}} \left[ \frac{1}{2} \|g(z; \theta_g)\|_{L^2(\Omega)}^2 - \langle g(z; \theta_g), u \rangle_{L^2(\Omega)} \right] + \beta D_{\text{KL}}(\mathbb{Q}_{z|u} \| \mathbb{P}_z), \end{aligned} \quad (5.1)$$

where  $\beta > 0$  is a hyperparameter. Analogously to (2.3), when  $\beta = 1$ , this ELBO is viewed as satisfying the equality

$$\log \frac{d\mathbb{P}_u}{d\mathbb{P}_\eta}(u; \theta_f, \theta_g, \beta) = D_{\text{KL}}(\mathbb{Q}_{z|u}^{\theta_f} \parallel \mathbb{P}_{z|u}^{\theta_g}) + \mathcal{L}_{\text{VANO}}(u; \theta_f, \theta_g, \beta),$$

and the quantity  $\log \frac{d\mathbb{P}_u}{d\mathbb{P}_\eta}(u)$  is interpreted as an analogue of the log-likelihood of the data  $u$  under the model. Even if the per-sample loss (5.1) makes sense for each  $u \in \mathcal{U}$ , further justification is needed to ensure that the expectation over the data  $u \sim \Upsilon$  is finite in light of the issues raised in Section 3. Indeed, the datasets considered by Seidman et al. (2023) all have at least  $L^2$ -regularity, meaning that the underlying data distribution  $\Upsilon$  is mutually singular with the decoder noise distribution  $\mathbb{P}_\eta$ ; thus, the finite-information condition (3.1) must fail and there is ambiguity in the probabilistic interpretation of their loss.

To avoid such ambiguities, we develop our theory around the underlying population loss, taking care to ensure that it is defined at the continuum before discretising, which necessarily results in our FVAE being restricted to data measures having finite information with respect to the decoder noise. To maximise the applicability of FVAE, we allow greater freedom in the choice of decoder noise compared to VANO and find that a well-chosen noise distribution can lead to significant improvements in the generative model (Section 2.5.1).

To explain the empirical successes of VANO despite the foundational challenges, we reinterpret the VANO objective through the lens of Section 4 as a regularised autoencoder similar to FAE, with the major difference in the formulation being whether the encoder returns a point or a distribution. Along with the differences in the underlying training objective and its interpretation, our work differs substantially in architecture and training procedure. While the VANO decoders can be discretised on any mesh—and, indeed, our proposed decoder (Section 2.4.3) closely resembles their nonlinear decoder—the encoders used by Seidman et al. (2023) assume a fixed mesh for all inputs at training and inference time. In contrast, our encoder (Section 2.4.2) can be discretised on any mesh; it is this combination of a discretisation-invariant encoder and decoder which enables many of our novel contributions, e.g., self-supervised training, inpainting, and superresolution.

**Generative models on function space.** Aside from VANO, recent years have seen significant interest in extending generative models to function space. Several extensions of score-based (Song et al., 2021) and denoising diffusion models (Sohl-Dickstein et al., 2015; Ho et al., 2020) to function space have been proposed (see, e.g., Pidstrigach et al., 2023; Hagemann et al., 2023; Lim et al., 2023; Kerrigan et al., 2023; Zhang and Wonka, 2024). Rahman et al. (2022) propose the generative adversarial neural operator, which extends the formulation of Wasserstein generative adversarial networks (Arjovsky et al., 2017) to function space and uses FNOs in the generator and discriminator networks to achieve resolution-invariance. These methods are united by the aim of pushing forward a Gaussian random field using an operator, whereas generative models based on autoencoders involve the pushforward of a Gaussian distribution on the *finite-dimensional* latent space; as discussed in Section 4.3.2, our approach has the benefit of being able to straightforwardly generate and refine a single sample at any resolution.

**Unsupervised learning on point clouds.** As discussed in Section 2.4, our architecture takes inspiration from the growing literature on machine learning on point clouds, where

the data are viewed as sets of points which could have arbitrary cardinality. A variety of models for autoencoding and generative modelling on point clouds have been proposed, such as energy-based processes (Yang et al., 2020) and SetVAE (Kim et al., 2021). Our approach differs from these methods by formulating a well-defined loss at the function-space level, ensuring that our model converges to a well-defined continuum limit as the mesh is refined.

## 6 Outlook

Our study of autoencoders on function space has led to FVAE, which imposes stringent requirements on the data distribution in infinite dimensions but benefits from firm probabilistic foundations, and the non-probabilistic FAE, which can be applied much more broadly. For both models, pairing the function-space objective with an encoder and decoder that can be discretised on arbitrary and distinct meshes has significant practical benefit, enabling training with heterogeneous data, inpainting, superresolution, and generative modelling.

**Limitations.** Owing to the need to satisfy the finite-information condition (3.1), FVAE applies only when the data measure is sufficiently close to being Gaussian. This condition may be impossible to satisfy or onerous to verify, and is a fundamental barrier to applying any VAE in infinite dimensions. FAE is an alternative autoencoding method in function space to overcome this, but it does not share the probabilistic foundations of FVAE.

The desire to discretise the encoder and decoder on arbitrary meshes rules out many high-performing architectures, including convolutional networks and FNOs. We believe this is the limiting factor in the experiments of Section 4.3, and that combining our work with more complex mesh-invariant architectures (e.g., Kovachki et al., 2023) or continuum extensions of point-cloud CNNs (Li et al., 2018) would yield further improvements.

**Future work.** Our work gives new methods for nonlinear dimension reduction in function space, and we expect there to be benefit in building operator-learning methods that make use of the resulting latent space, in the spirit of PCA-Net (Bhattacharya et al., 2021). For FAE, which unlike FVAE is not inherently a generative model, we anticipate particular benefit in the use of more sophisticated generative models on the latent space, for example diffusion models, analogous to Stable Diffusion (Rombach et al., 2022).

While our focus has been on scientific problems with synthetic data, our methodology could also be applied to real-world data, for example in computer vision. We expect that improved mesh-invariant architectures will be increasingly important in these applications.

## Acknowledgments and Disclosure of Funding

JB is supported by Splunk Inc. MG is supported by a Royal Academy of Engineering Research Chair, and Engineering and Physical Sciences Research Council (EPSRC) grants EP/T000414/1, EP/W005816/1, EP/V056441/1, EP/V056522/1, EP/R018413/2, EP/R034710/1, and EP/R004889/1. HL is supported by the Warwick Mathematics Institute Centre for Doctoral Training and gratefully acknowledges funding from the University of Warwick and the EPSRC (grant EP/W524645/1). AMS is supported by a Department of Defense Vannevar Bush Faculty Fellowship and by the SciAI Center, funded by the Office

of Naval Research (ONR), under grant N00014-23-1-2729. For the purpose of open access, the authors have applied a Creative Commons Attribution (CC BY) licence to any Author Accepted Manuscript version arising.

## References

- M. Arjovsky, S. Chintala, and L. Bottou. Wasserstein generative adversarial networks. In D. Precup and Y. W. Teh, editors, *Proceedings of the 34th International Conference on Machine Learning (ICML 2017)*, volume 70 of *Proceedings of Machine Learning Research*, pages 214–223, 2017. arXiv:1701.07875.
- K. Azzadenesheli, N. Kovachki, Z. Li, M. Liu-Schiaffini, J. Kossaifi, and A. Anandkumar. Neural operators for accelerating scientific simulations and design. *Nat. Rev. Phys.*, 6: 320–328, 2024. doi:10.1038/s42254-024-00712-5.
- K. Bhattacharya, B. Hosseini, N. B. Kovachki, and A. M. Stuart. Model reduction and neural networks for parametric PDEs. *SMAI J. Comput. Math.*, 7:121–157, 2021. doi:10.5802/smai-jcm.74.
- T. Bischoff and K. Deck. Unpaired downscaling of fluid flows with diffusion bridges. *Artif. Intell. Earth Syst.*, 3:e230039, 22pp., 2024. doi:10.1175/AIES-D-23-0039.1.
- C. M. Bishop. *Pattern Recognition and Machine Learning*. Information Science and Statistics. Springer, 2006. ISBN 978-0-387-31073-2.
- V. I. Bogachev. *Gaussian Measures*, volume 62 of *Mathematical Surveys and Monographs*. American Mathematical Society, 1998. doi:10.1090/surv/062.
- K. M. Borgwardt, A. Gretton, M. J. Rasch, H.-P. Kriegel, B. Schölkopf, and A. J. Smola. Integrating structured biological data by kernel maximum mean discrepancy. *Bioinform.*, 22(14):e49–e57, 2006. doi:10.1093/bioinformatics/btl242.
- D. R. Burt, S. W. Ober, A. Garriga-Alonso, and M. van der Wilk. Understanding variational inference in function-space. In *3rd Symposium on Advances in Approximate Bayesian Inference*, 2021. arXiv:2011.09421.
- E. Calvello, N. B. Kovachki, M. E. Levine, and A. M. Stuart. Continuum attention for neural operators, 2024. arXiv:2406.06486.
- G. J. Chandler and R. R. Kerswell. Invariant recurrent solutions embedded in a turbulent two-dimensional Kolmogorov flow. *J. Fluid. Mech.*, 722:554–595, 2013. doi:10.1017/jfm.2013.122.
- T. Chen and H. Chen. Approximations of continuous functionals by neural networks with application to dynamic systems. *IEEE Transactions on Neural Networks*, 4(6):910–918, 1993. doi:10.1109/72.286886.
- T. Cinquin and R. Bamler. Regularized KL-divergence for well-defined function-space variational inference in Bayesian neural networks, 2024. arXiv:2406.04317.

- S. L. Cotter, M. Dashti, and A. M. Stuart. Approximation of Bayesian inverse problems for PDEs. *SIAM J. Numer. Anal.*, 48(1):322–345, 2010. doi:10.1137/090770734.
- S. L. Cotter, G. O. Roberts, A. M. Stuart, and D. White. MCMC methods for functions: Modifying old algorithms to make them faster. *Statistical Science*, 28(3), 2013. doi:10.1214/13-STS421.
- W. M. Czarnecki, S. Osindero, M. Jaderberg, G. Swirszcz, and R. Pascanu. Sobolev training for neural networks. In I. Guyon, U. von Luxburg, S. Bengio, H. Wallach, R. Fergus, S. Vishwanathan, and R. Garnett, editors, *Advances in Neural Information Processing Systems*, volume 30, pages 4278–4287, 2017. ISBN 9781510860964. arXiv:1706.04859.
- M. Dashti and A. M. Stuart. The Bayesian approach to inverse problems. In *Handbook of Uncertainty Quantification. Vol. 1, 2, 3*, chapter 7, pages 311–428. Springer, Cham, 2017. doi:10.1007/978-3-319-12385-1\_7.
- J. Devlin, M.-W. Chang, K. Lee, and K. Toutanova. BERT: Pre-training of deep bidirectional transformers for language understanding. In J. Burstein, C. Doran, and T. Solorio, editors, *Proceedings of the 2019 Conference of the North American Chapter of the Association for Computational Linguistics: Human Language Technologies, Volume 1 (Long and Short Papers)*, pages 4171–4186, Minneapolis, MN, 2019. Association for Computational Linguistics. doi:10.18653/v1/N19-1423.
- W. E, W. Ren, and E. Vanden-Eijnden. Minimum action method for the study of rare events. *Comm. Pure Appl. Math.*, 57(5):637–656, 2004. doi:10.1002/cpa.20005.
- H. Edwards and A. Storkey. Towards a neural statistician. In *The Fifth International Conference on Learning Representations (ICLR 2017)*, 2017. arXiv:1606.02185.
- L. Evans. *Partial Differential Equations*, volume 19 of *Graduate Studies in Mathematics*. American Mathematical Society, 2nd edition, 2010. doi:10.1090/gsm/019.
- R. A. Freeze and J. A. Cherry. *Groundwater*. Prentice-Hall, Englewood Cliffs, NJ, 1979. ISBN 0-13-365312-9.
- S. Ghosal and A. van der Vaart. *Fundamentals of Nonparametric Bayesian Inference*. Cambridge University Press, first edition, 2017. doi:10.1017/9781139029834.
- P. Ghosh, M. S. M. Sajjadi, A. Vergari, M. Black, and B. Schölkopf. From variational to deterministic autoencoders. In *The Eighth International Conference on Learning Representations (ICLR 2020)*, 2020. arXiv:1903.12436.
- P. Hagemann, L. Ruthotto, G. Steidl, and N. T. Yang. Multilevel diffusion: Infinite dimensional score-based diffusion models for image generation, 2023. arXiv:2303.04772.
- M. Hairer, A. Stuart, and J. Voss. Signal processing problems on function space: Bayesian formulation, stochastic PDEs and effective MCMC methods. In *The Oxford Handbook of Nonlinear Filtering*, pages 833–873. Oxford University Press, Oxford, 2011. ISBN 9780199532902.

- K. He, X. Chen, S. Xie, Y. Li, P. Dollár, and R. Girshick. Masked autoencoders are scalable vision learners. In *2022 IEEE/CVF Conference on Computer Vision and Pattern Recognition (CVPR)*, pages 15979–15988, New Orleans, LA, USA, 2022. IEEE. doi:10.1109/CVPR52688.2022.01553. arXiv:2111.06377.
- D. Hendrycks and K. Gimpel. Gaussian error linear units (GELUs), 2016. arXiv:1606.08415.
- J. Ho, A. Jain, and P. Abbeel. Denoising diffusion probabilistic models. In H. Larochelle, M. Ranzato, R. Hadsell, M. F. Balcan, and H. Lin, editors, *Advances in Neural Information Processing Systems*, volume 33, pages 6840–6851. Curran Associates, Inc., 2020. ISBN 9781713829546. arXiv:2006.11239.
- D. Z. Huang, N. H. Nelsen, and M. Trautner. An operator learning perspective on parameter-to-observable maps, 2024. arXiv:2402.06031.
- B. E. Husic and V. S. Pande. Markov state models: From an art to a science. *J. Am. Chem. Soc.*, 140(7):2386–2396, 2018. doi:10.1021/jacs.7b12191.
- J. B. Keller. Darcy’s law for flow in porous media and the two-space method. In *Non-linear Partial Differential Equations in Engineering and Applied Science*, pages 429–443. Routledge, 1980. doi:10.1201/9780203745465-27.
- G. Kerrigan, J. Ley, and P. Smyth. Diffusion generative models in infinite dimensions. In F. Ruiz, J. Dy, and J.-W. van de Meent, editors, *Proceedings of the 26th International Conference on Artificial Intelligence and Statistics (AISTATS 2023)*, volume 206 of *Proceedings of Machine Learning Research*, pages 9538–9563, 2023. arXiv:2212.00886.
- J. Kim, J. Yoo, J. Lee, and S. Hong. SetVAE: Learning hierarchical composition for generative modeling of set-structured data. In *2021 IEEE/CVF Conference on Computer Vision and Pattern Recognition (CVPR)*, pages 15054–15063. IEEE, 2021. doi:10.1109/CVPR46437.2021.01481.
- D. P. Kingma and J. L. Ba. Adam: A method for stochastic optimization. In J. Bengio and Y. LeCun, editors, *The Third International Conference on Learning Representations (ICLR 2015)*, 2015. arXiv:1412.6980.
- D. P. Kingma and M. Welling. Auto-encoding variational Bayes. In Y. Bengio and Y. LeCun, editors, *The Second International Conference on Learning Representations (ICLR 2014)*, 2014. arXiv:1312.6114.
- D. Kochkov, J. A. Smith, A. Alieva, Q. Wang, M. P. Brenner, and S. Hoyer. Machine learning–accelerated computational fluid dynamics. *Proc. Nat. Acad. Sci. USA*, 118(21):e2101784118, 8pp., 2021. doi:10.1073/pnas.2101784118.
- K. A. Kononov, I. C. Unarta, S. Cao, E. C. Goonetilleke, and X. Huang. Markov state models to study the functional dynamics of proteins in the wake of machine learning. *J. Amer. Chem. Soc. Au*, 1(9):1330–1341, 2021. doi:10.1021/jacsau.1c00254.

- N. Kovachki, Z. Li, B. Liu, K. Azizzadenesheli, K. Bhattacharya, A. Stuart, and A. Anandkumar. Neural operator: Learning maps between function spaces with applications to PDEs. *J. Mach. Learn. Res.*, 23:1–97, 2023. arXiv:2108.08481.
- S. G. Krein and Yu. I. Petunin. Scales of Banach spaces. *Russ. Math. Surv.*, 21(2):85–159, 1966. doi:10.1070/RM1966v021n02ABEH004151.
- S. Lanthaler, A. M. Stuart, and M. Trautner. Discretization error of Fourier neural operators, 2024. arXiv:2405.02221.
- S. Lee. Mesh-independent operator learning for partial differential equations. In *2nd AI4Science Workshop at the 39th International Conference on Machine Learning*, 2022. URL <https://openreview.net/pdf?id=JUtzG8-2vGp>.
- J. Li, Z. Pei, W. Li, G. Gao, L. Wang, Y. Wang, and T. Zeng. A systematic survey of deep learning-based single-image super-resolution. *ACM Comput. Surv.*, 56(10):1–40, 2024. doi:10.1145/3659100.
- Y. Li, R. Bu, M. Sun, W. Wu, X. Di, and B. Chen. PointCNN: Convolution on  $\mathcal{X}$ -transformed points. In S. Bengio, H. Wallach, H. Larochelle, K. Grauman, N. Cesa-Bianchi, and R. Garnett, editors, *Advances in Neural Information Processing Systems*, volume 31, pages 820–830. Curran Associates, Inc., 2018. ISBN 9781510884472. arXiv:1801.07791.
- Z. Li, N. Kovachki, K. Azizzadenesheli, B. Liu, K. Bhattacharya, A. Stuart, and A. Anandkumar. Fourier neural operator for parametric partial differential equations. In *The Ninth International Conference on Learning Representations (ICLR 2021)*, 2021. arXiv:2010.08895.
- J. H. Lim, N. B. Kovachki, R. Baptista, C. Beckham, K. Azizzadenesheli, J. Kossaifi, V. Voleti, J. Song, K. Kreis, J. Kautz, C. Pal, A. Vahdat, and A. Anandkumar. Score-based diffusion models in function space, 2023. arXiv:2302.07400.
- R. S. Liptser and A. N. Shiryaev. *Statistics of Random Processes*. Springer, Berlin, Heidelberg, 2001. doi:10.1007/978-3-662-13043-8.
- L. Lu, P. Jin, G. Pang, Z. Zhang, and G. E. Karniadakis. Learning nonlinear operators via DeepONet based on the universal approximation theorem of operators. *Nat. Mach. Intell.*, 3(3):218–229, 2021. doi:10.1038/s42256-021-00302-5.
- A. Mardt, L. Pasquali, H. Wu, and F. Noé. VAMPnets for deep learning of molecular kinetics. *Nat. Commun.*, 9(1):5, 11pp., 2018. doi:10.1038/s41467-017-02388-1.
- F. Nüske, H. Wu, J.-H. Prinz, C. Wehmeyer, C. Clementi, and F. Noé. Markov state models from short non-equilibrium simulations—analysis and correction of estimation bias. *J. Chem. Phys.*, 146(9):094104, 16pp., 2017. doi:10.1063/1.4976518.
- B. Øksendal. *Stochastic Differential Equations*. Universitext. Springer, Berlin, Heidelberg, 2003. doi:10.1007/978-3-642-14394-6.



- B. Peherstorfer. Breaking the Kolmogorov barrier with nonlinear model reduction. *Not. Am. Math. Soc.*, 69(5):725–733, 2022. doi:10.1090/noti2475.
- J. Pidstrigach, Y. Marzouk, S. Reich, and S. Wang. Infinite-dimensional diffusion models for function spaces, 2023. arXiv:2302.10130.
- M. Prasthofer, T. De Ryck, and S. Mishra. Variable-input deep operator networks, 2022. arXiv:2205.11404.
- J.-H. Prinz, H. Wu, M. Sarich, B. Keller, M. Senne, M. Held, J. D. Chodera, C. Schütte, and F. Noé. Markov models of molecular kinetics: Generation and validation. *J. Chem. Phys.*, 134(17):174105, 23pp., 2011. doi:10.1063/1.3565032.
- C. R. Qi, H. Su, K. Mo, and L. J. Guibas. PointNet: Deep learning on point sets for 3D classification and segmentation. In *2017 IEEE Conference on Computer Vision and Pattern Recognition (CVPR)*, pages 77–85. IEEE, 2017. doi:10.1109/CVPR.2017.16.
- W. Quan, J. Chen, Y. Liu, D.-M. Yan, and P. Wonka. Deep learning-based image and video inpainting: A survey. *Int. J. Comput. Vis.*, 132:2364–2400, 2024. doi:10.1007/s11263-023-01977-6.
- M. A. Rahman, M. A. Florez, A. Anandkumar, Z. E. Ross, and K. Azizzadenesheli. Generative adversarial neural operators. *Transact. Mach. Learn. Res.*, 2022. arXiv:2205.03017.
- J. O. Ramsay and B. W. Silverman, editors. *Applied Functional Data Analysis: Methods and Case Studies*. Springer Series in Statistics. Springer, 2002. doi:10.1007/b98886.
- R. Rombach, A. Blattmann, D. Lorenz, P. Esser, and B. Ommer. High-resolution image synthesis with latent diffusion models. In *2022 IEEE/CVF Conference on Computer Vision and Pattern Recognition (CVPR)*, pages 10674–10685, New Orleans, LA, USA, 2022. IEEE. doi:10.1109/CVPR52688.2022.01042.
- S. Särkkä and A. Solin. *Applied Stochastic Differential Equations*. Cambridge University Press, first edition, 2019. doi:10.1017/9781108186735.
- T. Schlick. *Molecular Modeling and Simulation: An Interdisciplinary Guide*, volume 21 of *Interdisciplinary Applied Mathematics*. Springer, New York, second edition, 2010. doi:10.1007/978-1-4419-6351-2.
- D. W. Scott. *Multivariate Density Estimation*. Wiley Series in Probability and Statistics. John Wiley and Sons, second edition, 2015. doi:10.1002/9781118575574.
- J. H. Seidman, G. Kissas, P. Perdikaris, and G. J. Pappas. NOMAD: Nonlinear manifold decoders for operator learning. In S. Koyejo, S. Mohamed, A. Agarwal, D. Belgrave, K. Cho, and A. Oh, editors, *Advances in Neural Information Processing Systems*, volume 35, pages 5601–5613. Curran Associates, Inc., 2022. ISBN 9781713871088.
- J. H. Seidman, G. Kissas, G. J. Pappas, and P. Perdikaris. Variational autoencoding neural operators. In A. Krause, E. Brunskill, K. Cho, B. Engelhardt, S. Sabato, and J. Scarlett, editors, *Proceedings of the 40th International Conference on Machine Learning (ICML)*

- 2023), volume 202 of *Proceedings of Machine Learning Research*, pages 30491–30522, 2023. arXiv:2302.10351.
- K. Simonyan and A. Zisserman. Very deep convolutional networks for large-scale image recognition. In J. Bengio and Y. LeCun, editors, *The Third International Conference on Learning Representations (ICLR 2015)*, 2015. arXiv:1409.1556.
- V. Sitzmann, J. N. P. Martel, A. W. Bergman, D. B. Lindell, and G. Wetzstein. Implicit neural representations with periodic activation functions. In H. Larochelle, M. Ranzato, R. Hadsell, M. F. Balcan, and H. Lin, editors, *Advances in Neural Information Processing Systems*, volume 33, pages 7462–7473. Curran Associates, Inc., 2020. ISBN 9781713829546. arXiv:2006.09661.
- J. Sohl-Dickstein, E. Weiss, N. Maheswaranathan, and S. Ganguli. Deep unsupervised learning using nonequilibrium thermodynamics. In F. Bach and D. Blei, editors, *Proceedings of the 32nd International Conference on Machine Learning (ICML 2015)*, volume 37 of *Proceedings of Machine Learning Research*, pages 2256–2265, 2015. arXiv:1503.03585.
- Y. Song, J. Sohl-Dickstein, D. P. Kingma, A. Kumar, S. Ermon, and B. Poole. Score-based generative modeling through stochastic differential equations. In *The Ninth International Conference on Learning Representations (ICLR 2021)*, 2021. arXiv:2011.13456.
- A. M. Stuart. Inverse problems: A Bayesian perspective. *Acta Numer.*, 19:451–559, 2010. doi:10.1017/S0962492910000061.
- V. N. Sudakov. Linear sets with quasi-invariant measure. *Dokl. Akad. Nauk SSSR*, 127:524–525, 1959.
- S. Sun, G. Zhang, J. Shi, and R. Grosse. Functional variational Bayesian neural networks. In *The Seventh International Conference on Learning Representations (ICLR 2019)*, 2019. arXiv:1903.05779.
- M. Tancik, P. P. Srinivasan, B. Mildenhall, S. Fridovich-Keil, N. Raghavan, U. Singhal, R. Ramamoorthi, J. T. Barron, and R. Ng. Fourier features let networks learn high frequency functions in low dimensional domains. In H. Larochelle, M. Ranzato, R. Hadsell, M. F. Balcan, and H. Lin, editors, *Advances in Neural Information Processing Systems*, volume 33, pages 7537–7547. Curran Associates, Inc., 2020. ISBN 9781713829546. arXiv:2006.10739.
- A. Vahdat, K. Kreis, and J. Kautz. Score-based generative modeling in latent space. In M. Ranzato, A. Beygelzimer, Y. Dauphin, P. S. Liang, and J. Wortman Vaughan, editors, *Advances in Neural Information Processing Systems*, volume 34, pages 11287–11302. Curran Associates, Inc., 2021. ISBN 9781713845393. arXiv:2106.05931.
- A. Vaswani, N. Shazeer, N. Parmar, J. Uszkoreit, L. Jones, A. N. Gomez, L. Kaiser, and I. Polosukhin. Attention is all you need. In I. Guyon, U. von Luxburg, S. Bengio, H. Wallach, R. Fergus, S. Vishwanathan, and R. Garnett, editors, *Advances in Neural Information Processing Systems*, volume 30, pages 5998–6008, 2017. ISBN 9781510860964.

- M. Yang, B. Dai, H. Dai, and D. Schuurmans. Energy-based processes for exchangeable data. In H. Daumé III and A. Singh, editors, *Proceedings of the 37th International Conference on Machine Learning (ICML 2020)*, volume 119 of *Proceedings of Machine Learning Research*, pages 10681–10692, 2020. arXiv:2003.07521.
- M. Zaheer, S. Kottur, S. Ravanbakhsh, B. Póczos, R. Salakhutdinov, and A. J. Smola. Deep sets. In I. Guyon, U. von Luxburg, S. Bengio, H. Wallach, R. Fergus, S. Vishwanathan, and R. Garnett, editors, *Advances in Neural Information Processing Systems*, volume 30, pages 3391–3401, 2017. ISBN 9781510860964. arXiv:1703.06114.
- B. Zhang and P. Wonka. Functional diffusion. In *Proceedings of the IEEE/CVF Conference on Computer Vision and Pattern Recognition (CVPR)*, pages 4723–4732, 2024. arXiv:2311.15435.

## Appendix A. Supporting Results

### A.1 Supporting Results for Section 2

**Proof of Lemma 2.1** First, suppose that  $\mathbb{P}_u(A) = \int_{\mathcal{Z}} \mathbb{P}_{u|z}(A) \mathbb{P}_z(dz) = 0$ . Then,  $\mathbb{P}_z$ -almost surely,  $\mathbb{P}_{u|z}(A) = 0$ , and since  $\Upsilon \ll \mathbb{P}_{u|z}$  for all  $z \in \mathcal{Z}$ , we conclude that  $\Upsilon(A) = 0$ , i.e.,  $\Upsilon \ll \mathbb{P}_u$ . The fact that  $\mathbb{Q}_{z,u} \ll \mathbb{P}_{z,u}$  then follows from the factorisations (2.6)–(2.8), as does the expression for the joint density.  $\blacksquare$

A useful tool in deriving the ELBO (2.15) is the **data-processing inequality for KL divergence** (see, e.g., Burt et al., 2021, Proposition 1): given measurable spaces  $\mathcal{U}$  and  $\mathcal{V}$ , probability measures  $\mu$  and  $\nu$  on  $\mathcal{U}$ , and a measurable map  $g: \mathcal{U} \rightarrow \mathcal{V}$ , we have  $D_{\text{KL}}(g\# \mu \parallel g\# \nu) \leq D_{\text{KL}}(\mu \parallel \nu)$ .

**Proof of Theorem 2.2** By the data-processing inequality, since  $D_{\text{KL}}(\mathbb{Q}_{z,u} \parallel \mathbb{P}_{z,u}) < \infty$ , it follows that

$$D_{\text{KL}}(\Upsilon \parallel \mathbb{P}_u) = D_{\text{KL}}(\pi_{\sharp}^{\mathcal{U}} \mathbb{Q}_{z,u} \parallel \pi_{\sharp}^{\mathcal{U}} \mathbb{P}_{z,u}) \leq D_{\text{KL}}(\mathbb{Q}_{z,u} \parallel \mathbb{P}_{z,u}) < \infty. \quad (\text{A.1})$$

Thus, using the joint density from Lemma 2.1,

$$\begin{aligned} D_{\text{KL}}(\mathbb{Q}_{z,u} \parallel \mathbb{P}_{z,u}) &= \mathbb{E}_{u \sim \Upsilon} \mathbb{E}_{z \sim \mathbb{Q}_{z|u}} \left[ \log \frac{d\Upsilon}{d\mathbb{P}_u}(u) + \log \frac{d\mathbb{Q}_{z|u}}{d\mathbb{P}_{z|u}}(z; u) \right] \\ &= D_{\text{KL}}(\Upsilon \parallel \mathbb{P}_u) + \mathbb{E}_{u \sim \Upsilon} [D_{\text{KL}}(\mathbb{Q}_{z|u} \parallel \mathbb{P}_{z|u})], \end{aligned}$$

and all terms are finite as a consequence of (A.1).  $\blacksquare$

**Proof of Theorem 2.3** Again using Lemma 2.1, along with the fact that  $\Upsilon \ll \mathbb{P}_{u|z} \ll \mathbb{P}_\eta$  for all  $z \in \mathcal{Z}$ , we see that

$$\begin{aligned} D_{\text{KL}}(\mathbb{Q}_{z,u} \parallel \mathbb{P}_{z,u}) &= \mathbb{E}_{u \sim \Upsilon} \mathbb{E}_{z \sim \mathbb{Q}_{z|u}} \left[ \log \frac{d\Upsilon}{d\mathbb{P}_{u|z}}(u; z) + \log \frac{d\mathbb{Q}_{z|u}}{d\mathbb{P}_z}(z; u) \right] \\ &= \mathbb{E}_{u \sim \Upsilon} \mathbb{E}_{z \sim \mathbb{Q}_{z|u}} \left[ \log \frac{d\Upsilon}{d\mathbb{P}_\eta}(u) - \log \frac{d\mathbb{P}_{u|z}}{d\mathbb{P}_\eta}(u; z) + \log \frac{d\mathbb{Q}_{z|u}}{d\mathbb{P}_z}(z; u) \right] \\ &= D_{\text{KL}}(\Upsilon \parallel \mathbb{P}_\eta) + \mathbb{E}_{u \sim \Upsilon} \left[ \mathbb{E}_{z \sim \mathbb{Q}_{z|u}} \left[ -\log \frac{d\mathbb{P}_{u|z}}{d\mathbb{P}_\eta}(u; z) \right] + D_{\text{KL}}(\mathbb{Q}_{z|u} \parallel \mathbb{P}_z) \right]. \end{aligned}$$

Note that, since  $\mathbb{Q}_{z|u} = N(m(u; \theta_f), \Sigma(u; \theta_f))$  and  $\mathbb{P}_z = N(0, I_{d_{\mathcal{Z}}})$  are Gaussian on  $\mathcal{Z} = \mathbb{R}^{d_{\mathcal{Z}}}$ , the KL divergence  $D_{\text{KL}}(\mathbb{Q}_{z|u} \parallel \mathbb{P}_z)$  admits the analytical form

$$D_{\text{KL}}(\mathbb{Q}_{z|u} \parallel \mathbb{P}_z) = \frac{1}{2} \|m(u; \theta_f)\|_2^2 + \frac{1}{2} \text{tr} \Sigma(u; \theta_f) - \frac{d_{\mathcal{Z}}}{2} - \frac{1}{2} \log \det \Sigma(u; \theta_f) < \infty$$

Finiteness of each term thus follows from the hypotheses that  $D_{\text{KL}}(\mathbb{Q}_{z,u} \parallel \mathbb{P}_{z,u}) < \infty$  and  $D_{\text{KL}}(\Upsilon \parallel \mathbb{P}_\eta) < \infty$ , and the fact that  $D_{\text{KL}}(\mathbb{Q}_{z|u} \parallel \mathbb{P}_z) < \infty$ .  $\blacksquare$

**Lemma A.1** *Suppose that  $\mathcal{U} = C_0([0, T], \mathbb{R}^m)$  and that  $\mu \in \mathcal{P}(\mathcal{U})$  and  $\nu \in \mathcal{P}(\mathcal{U})$  are the laws of the  $\mathbb{R}^m$ -valued diffusions*

$$\begin{aligned} du_t &= b(u_t) dt + \sqrt{\varepsilon} dw_t, & u_0 &= 0, & t &\in [0, T] \\ dv_t &= c(v_t) dt + \sqrt{\varepsilon} dw_t, & v_0 &= 0, & t &\in [0, T]. \end{aligned}$$

where  $w_t$  is a Brownian motion on  $\mathbb{R}^m$ . Suppose that the Novikov condition (e.g., Øksendal, 2003, eq. (8.6.8)) holds for both processes, i.e.,

$$\mathbb{E}_{u \sim \mu} \left[ \frac{1}{2\varepsilon} \int_0^T \|b(u_t)\|_2^2 dt \right] < \infty \quad \text{and} \quad \mathbb{E}_{v \sim \nu} \left[ \frac{1}{2\varepsilon} \int_0^T \|c(v_t)\|_2^2 dt \right] < \infty.$$

Then

$$D_{\text{KL}}(\mu \parallel \nu) = \mathbb{E}_{u \sim \mu} \left[ \frac{1}{2\varepsilon} \int_0^T \|b(u_t) - c(u_t)\|_2^2 dt \right].$$

**Proof** As the Novikov condition is satisfied,  $\mu \sim \nu$  and the Girsanov formula yields

$$\frac{d\mu}{d\nu}(u) = \exp \left( \frac{1}{2\varepsilon} \int_0^T \|b(u_t) - c(u_t)\|_2^2 dt - \frac{1}{\varepsilon} \int_0^T b(u_t) - c(u_t) dW_t, \right) \quad (\text{A.2})$$

where  $W_t = w_t - \int_0^t b(u_s) ds$ . Thus, using (A.2) in the definition of the KL divergence,

$$D_{\text{KL}}(\mu \parallel \nu) = \mathbb{E}_{u \sim \mu} \left[ \frac{1}{2\varepsilon} \int_0^T \|b(u_t) - c(u_t)\|_2^2 dt - \frac{1}{\varepsilon} \int_0^T b(u_t) - c(u_t) dW_t \right].$$

The result follows as the stochastic integral is a martingale with zero expectation under  $\mu$ . ■

We point out that the Novikov condition in Lemma A.1 is merely used as a convenient sufficient condition to apply the Girsanov theorem, and more general conditions such as the Kazamaki condition (Liptser and Shiryaev, 2001, p. 249) could also be applied.

## A.2 Supporting Results for Section 4

**Proof of Proposition 4.1** This follows immediately from evaluating  $\mathcal{J}_{\text{FAE}}$  with parameters  $\theta_f$  and  $\theta_g$  such that  $f(u; \theta_f) = 0$  and  $g(z; \theta_g) = 0$ , since

$$\mathcal{J}_{\text{FAE}}(u; \theta_f, \theta_g, \beta) = \mathbb{E}_{u \sim \Upsilon} \left[ \frac{1}{2} \|u\|_{\mathcal{U}}^2 \right],$$

and the expectation is finite by hypothesis. ■

## Appendix B. Experimental Details

In this section, we provide additional details, training configurations, and analysis for the numerical experiments in Section 2.5 and Section 4.3. We also provide further samples and reconstructions from our learned FVAE and FAE models.

### B.1 Base Architecture

We use the common architecture described in Section 2.4 and Section 4.2 for all experiments.

**Positional encodings.** In each case, both the encoder and decoder may make use of Gaussian random Fourier features (Tancik et al., 2020), pairing the query coordinate  $x \in \Omega \subset \mathbb{R}^d$  with a positional encoding  $\gamma(x) \in \mathbb{R}^{2k}$ . To generate these encodings, a matrix  $B \in \mathbb{R}^{k \times d}$  with independent  $N(0, I)$  entries is sampled and viewed as a hyperparameter of the model to be used in both the encoder and decoder. The positional encoding  $\gamma(x)$  is then given by the concatenated vector

$$\gamma(x) = [\cos(2\pi Bx); \sin(2\pi Bx)]^T \in \mathbb{R}^{2k},$$

where the sine and cosine functions are applied componentwise to the vector  $2\pi Bx$ .

**Optimiser.** For all experiments we use the Adam optimiser (Kingma and Ba, 2015) with the default hyperparameters.

### B.2 Brownian Dynamics

The training data consists of 8,192 samples from the path measure  $\Upsilon$  of the SDE on the time interval  $[0, T]$ ,  $T = 5$ , at timestep  $5/512$ , with 50% of timesteps assumed to be missing in each sample. Trajectories are generated using the Euler–Maruyama scheme with internal timestep  $1/8192$ , and the resulting paths are then subsampled by a factor of 80 to obtain the training data.

**Experimental setup.** We train for 50,000 steps using an initial learning rate of  $10^{-3}$  with an exponential decay of 0.98 being applied every 1,000 steps. We use a batch size of 32 and take 4 Monte Carlo samples for  $\mathbb{Q}_{z|u}$ . We use the same base architecture described in Appendix B.1 but with a latent dimension  $d_Z = 1$ ,  $\beta = 1$  and  $\lambda = 10$ . The three models in Figure 2.2 use  $\theta = 0$ ,  $\theta = 25$  and  $\theta = 10,000$ , respectively.

### B.3 Estimation of Markov State Models

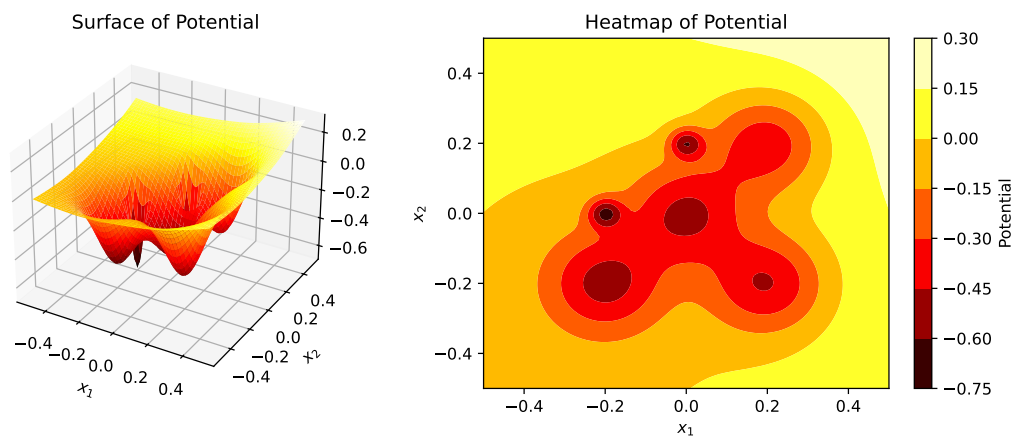


Figure B.1: Potential function  $U$  for Section 2.5.2, given by (B.1).

**Data and discretisation.** To validate the ability of FVAE to model higher-dimensional SDE trajectories, we specify a simple-to-visualise potential with qualitative features similar to those arising in the more complex potential surfaces arising in MD. To this end, define the centres  $c_1 = (0, 0)$ ,  $c_2 = (0.2, 0.2)$ ,  $c_3 = (-0.2, -0.2)$ ,  $c_4 = (0.2, -0.2)$ ,  $c_5 = (0, 0.2)$  and  $c_6 = (-0.2, 0)$ ; standard deviations  $\sigma_1 = \sigma_2 = \sigma_3 = \sigma_4 = 0.1$  and  $\sigma_5 = \sigma_6 = 0.03$ ; and masses  $m_1 = m_2 = m_3 = m_4 = 0.1$  and  $m_5 = m_6 = 0.01$ . Then let

$$U(x) = 0.3 \left[ 0.5(x_1 + x_2) + x_1^2 + x_2^2 - \sum_{i=1}^6 m_i N(x; c_i, \sigma_i^2 I_2) \right]. \quad (\text{B.1})$$

The potential (B.1) has three key components: a linear term breaking the symmetry, a quadratic term preventing paths from veering too far from the origin (i.e., the path’s starting point), and negative Gaussian densities—serving as potential wells—positioned at the centres  $c_i$  (Figure B.1). Sample paths with initial condition  $u_0 = 0$ , temperature  $\varepsilon = 0.1$  and final time  $T = 3$  show significant diversity, with many paths transitioning at least once between different wells (Figure B.3).

**Experimental setup.** The training set consists of 16,384 sample paths using an Euler–Maruyama scheme with timestep  $1/8,192$ , subsampling by a factor 48 to obtain an equally spaced mesh of 513 points. We adopt the base architecture described in Appendix B.1, with the SDE objective (Section 2.3.1) using latent dimension  $d_Z = 16$ ,  $\beta = 0.02$ ,  $\theta = 100$ , and  $\lambda = 50$ . We implement the same training strategy as described in Appendix B.3 by training on data where 50% of the points on the path are missing. We also use the same learning rate, learning rate decay schedule, maximum number of steps, and batch size.

**Results.** FVAE produces convincing samples and reconstructions (Figures B.2 and B.3).

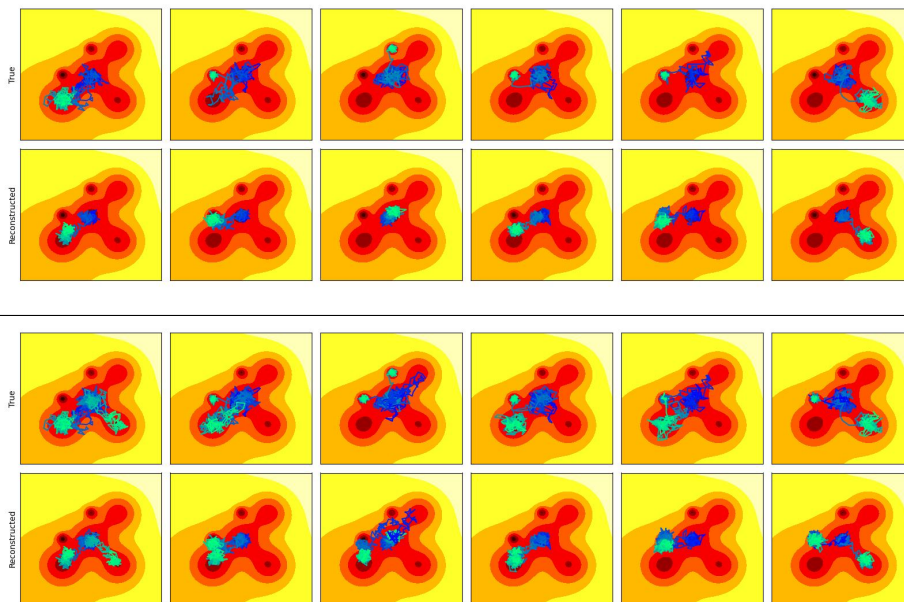
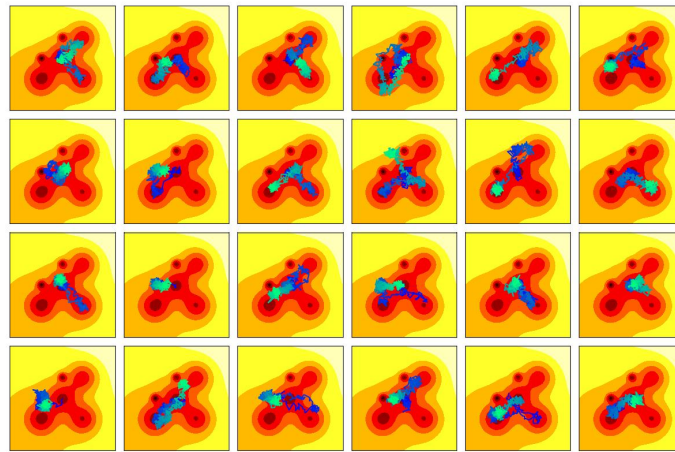
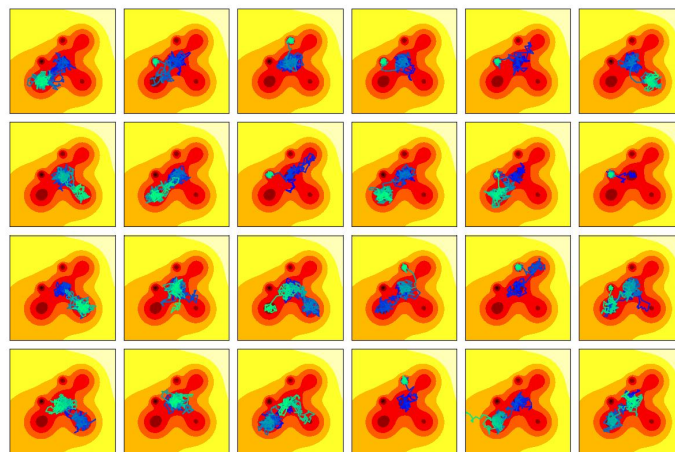


Figure B.2: Reconstructions of sample paths from the SDE in Section 2.5.2.



(a) FVAE



(b) Dataset

Figure B.3: Samples of the SDE in Section 2.5.2, where the evolution through time  $t \in [0, 3]$  is depicted as a transition in colour from blue to green.



### B.4 Dirac Distributions

**Data and discretisation.** We view the data measure  $\Upsilon$  as a probability measure on the space  $\mathcal{U} = H^{-1}((0, 1))$ . At each resolution, we discretise the domain  $(0, 1)$  using an evenly spaced mesh of points and approximate the Dirac mass  $\delta_\theta$ ,  $\theta \in (0, 1)$ , by the optimal  $L^1$ -approximation: a discretised function which is zero except at the mesh point closest to  $\theta$ , normalised to have unit  $L^1$ -norm. The training dataset consists of a Dirac function centred at each mesh point; we emphasise the goal is not to train a practical model for generalisation, but to isolate the effect of the population loss.

**Experimental setup.** We train both the FVAE model and the FAE model at resolutions 8, 16, 32, 64, and 128. For both models, we train for 30,000 steps with a batch size of 6. At each resolution, we perform 50 runs using different random seeds.

**Architecture.** To isolate the effect of the ill-defined ELBO, and to avoid issues associated with operating on functions of negative Sobolev regularity, we define an encoder and decoder architecture tailored to this problem. As in Section 2.4.2, we restrict to the case that the covariance matrix learned by the encoder is diagonal, and take

$$\tilde{f}(u; \theta_f) = \rho \left( \arg \max_{x \in [0, 1]} (\varphi * u)(x); \theta_f \right),$$

where  $\rho: \mathbb{R} \times \Theta_f \rightarrow \mathbb{R} \times \mathbb{R}$  is a neural network with 3 hidden layers of width 128 and  $\varphi: \mathbb{R} \rightarrow \mathbb{R}$  is some compactly supported smooth mollifier, chosen such that  $\varphi * u$  is smooth and the maximum is well-defined. The decoder is chosen to return the Gaussian density

$$g(z; \theta_g)(x) = N \left( \mu(z; \theta_g), \sigma(z; \theta_g)^2; x \right),$$

with learnable mean  $\mu(z; \theta_g)$  and standard deviation  $\sigma(z; \theta_g)$  computed from a 3-layer neural network of width 128. For numerical stability, we impose a lower bound on  $\sigma$  based on the mesh spacing  $\Delta x$ , given by  $\sigma_{\min}(\Delta x) := (2\pi)^{-1/2} \Delta x$ .

**FVAE configuration.** We take decoder noise distribution  $\mathbb{P}_\eta = N(0, I)$  on  $L^2((0, 1))$ , with  $\mathbb{P}_\eta \in \mathcal{P}(H^{-s}((0, 1)))$ ,  $s < -1/2$ . We modify the FVAE objective (2.13) by reweighting the term  $D_{\text{KL}}(\mathbb{Q}_{z|u} \| \mathbb{P}_z)$  by  $\beta = 10^{-4}$ , and take 16 Monte Carlo samples for  $\mathbb{Q}_{z|u}$ . We use an initial learning rate of  $10^{-4}$ , decaying exponentially by a factor 0.7 every 1,000 steps.

**FAE configuration.** For the FAE objective (4.1), we discretise the  $H^{-1}$ -norm, viewed as a weighted sum of frequencies (see, e.g., Krein and Petunin, 1966, Sec. 9), as

$$\|u\|_{H^{-1}((0, 1))}^2 \approx \sum_{j=1}^n (1 + j^2)^{-1} |\alpha_j|^2, \quad u = \sum_{j \in \mathbb{N}} \alpha_j e_j, \quad e_j(x) = \sqrt{2} \sin(\pi j x),$$

with the coefficients  $\alpha_i$  calculated from a discretisation of  $u$  using the discrete sine transform. We use an initial learning rate of  $10^{-4}$  decaying exponentially by a factor 0.9 every 1,000 steps, and take  $\beta = 10^{-12}$ .

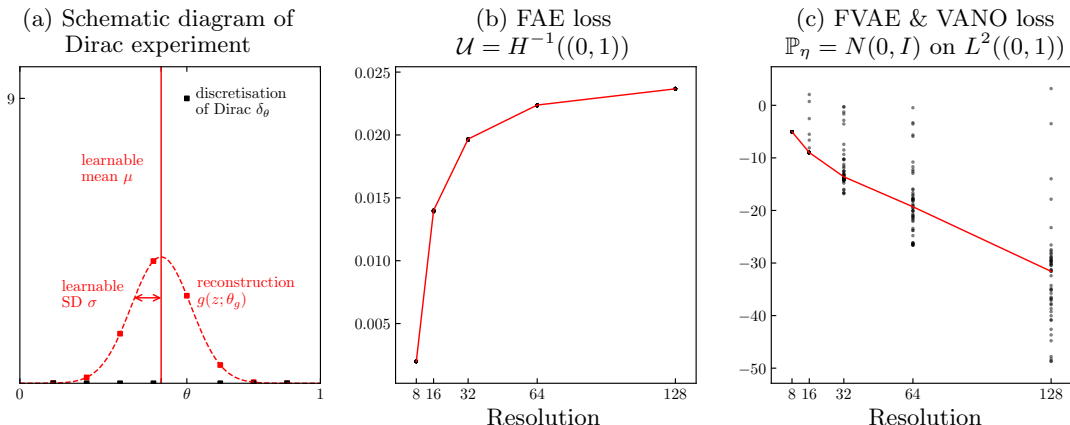


Figure B.4: (a): The discrete representations (squares) of  $\delta_\theta$  and  $g(z; \theta_g)$  on a grid of 8 points. (b) and (c): By discretising the two losses at an increasing sequence of resolutions, we see that the FAE loss rapidly converges, whereas a doubling of resolution approximately leads to a doubling of the FVAE loss, suggesting the continuum limit is infinite. Each dot in (b) and (c) represents one of 50 training runs with distinct random seed, with the red line connecting the medians.

**Results.** As expected, the final training loss under both models decreases as the resolution is refined, since the lower bound  $\sigma_{\min}$  decreases. The striking difference, however, is that the FAE loss appears to converge and is stable across runs, while the FVAE loss appears to diverge and becomes increasingly unstable across runs. This provides convincing empirical evidence that the underlying population loss for FVAE is not defined as a result of the misspecified decoder noise; the use of FAE with an appropriate data norm alleviates this issue. Since the FVAE objective with  $\mathbb{P}_\eta = N(0, I)$  coincides with the VANO objective, this issue would also be present for VANO. We point out that, under both models, training becomes increasingly unstable at high resolutions: when  $\sigma$  is small, the loss becomes extremely sensitive to changes in  $\mu$ ; this instability is unrelated to the divergence of the FVAE training loss and is instead a consequence of training through gradient descent.

## B.5 Navier–Stokes Equations

Viscosity $\nu$	Resolution	# Train	# Eval.	Snapshot Time $T$
$10^{-3}$	$64 \times 64$	4,000	1,000	50
$10^{-4}$	$64 \times 64$	8,000	2,000	50
$10^{-5}$	$64 \times 64$	960	240	20

Table B.1: Details of Navier–Stokes datasets.

**Data and discretisation.** The data used here was provided online by Li et al. (2021). Solutions from (4.2) are generated numerically by first sampling the initial condition from

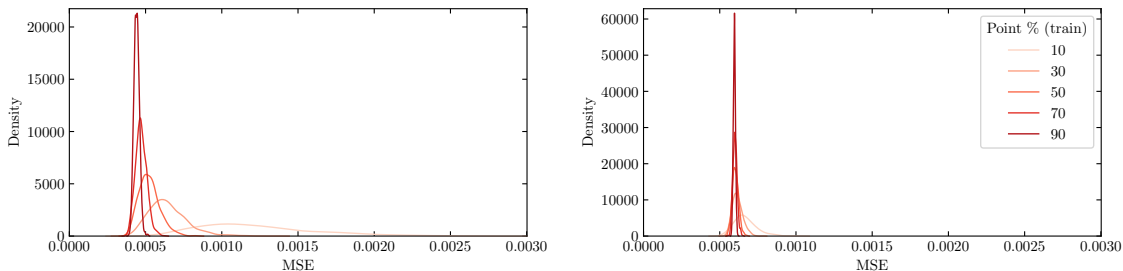
the Gaussian random field  $N(0, C)$ ,  $C = 7^{3/2}(49I - \Delta)^{-5/2}$  and then performing the time evolution using a pseudospectral method, as described by Li et al. (2021).

While the data of Li et al. (2021) includes the full time evolution, we use only snapshots of the solution vorticity field at the final timestep. Every snapshot is a  $64 \times 64$  image, normalised to take values in  $[0, 1]$  using the minimum and maximum across all the data. The details of this dataset can be found in Table B.1.

**Effects of point ratios.** As described in Section 2.4.4, the self-supervised training scheme we adopt involves masking a fixed proportion of randomly selected points before encoding, and then decoding only on the masked mesh points. We call the proportion of points available to the encoder the **(encoder) point ratio**, which serves as an additional hyperparameter of FVAE and FAE. Here, we extend the analysis of Figure 4.2(b) for FAE to understand how the point ratio during training affects the reconstruction performance.

We first train two FAE models on the Navier–Stokes dataset with viscosity  $\nu = 10^{-4}$ , using encoder point ratio 10% and 90% respectively. Selecting an arbitrary sample from the held-out set, we draw 1,000 distinct meshes with specified point ratio, evaluate the encoder on each of these meshes, and then decode on the full mesh, using the reconstruction MSE on the full grid to evaluate performance. Using the same procedure as in Section 2.5.1, we construct a kernel density estimate of the resulting distribution of reconstruction MSEs, shown in Figure B.5 for both models.

We find that the model trained with encoder point ratio 10% is much more sensitive to the location of the evaluation mesh points, especially when the evaluation point ratio is low. With sufficiently high encoder point ratio at evaluation time, however, the reconstruction MSE of the model trained using point ratio 10% surpasses that of the model trained at 90%. This suggests a tradeoff whereby a higher training point ratio provides more stability, with the price to be paid being an increase in autoencoding MSE, particular when the point ratio of the evaluation data is high. We hypothesise that a lower training ratio implicitly regularises the model to attain a more robust internal representation.

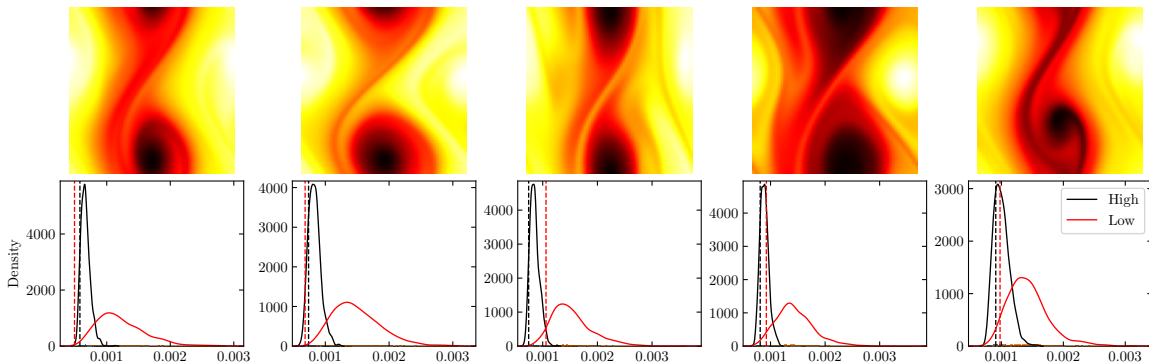


(a) For a model trained with point ratio 10%. (b) For a model trained with a point ratio 90%.

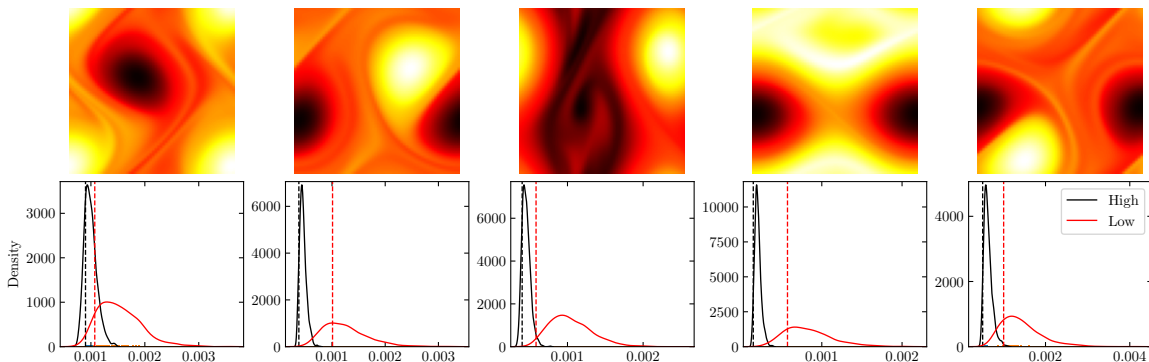
Figure B.5: Kernel density estimates for full-grid reconstruction MSE on the reference sample across 1,000 randomly chosen meshes. Training with a low point ratio regularises, reducing MSE when the evaluation data has a high point ratio, but at the cost of greater variance when evaluating on low point ratios.

We also investigate the sensitivity of the models to a specific encoder mesh, seeking to understand whether an encoder mesh achieving low MSE on one image leads to low MSE on

other images. The procedure is as follows: we select an image arbitrarily from the held-out set (the **reference sample**) and draw 1,000 random meshes with point ratio 10%; then, we select the mesh resulting in the lowest reconstruction MSE for each of the two models. For the nearest neighbours of the chosen sample in the held-out set, the reconstruction error on this MSE-minimising mesh is lower than average (Figure B.6(a); dashed lines), suggesting that a good configuration will yield good results on similar samples. On the other hand, using the MSE-minimising mesh on arbitrary samples from the held-out set yields an MSE somewhat lower than a randomly chosen mesh; unsurprisingly, however, the arbitrarily chosen samples appear to benefit less than the nearest neighbours (Figure B.6(b)).



(a) Nearest neighbours of the reference sample in the held-out set.



(b) Arbitrarily chosen samples from the held-out set.

Figure B.6: Kernel density estimates of full-grid reconstruction MSE for models trained at 10% (Low) and 90% (High) point ratios on samples from the held-out set. Dashed lines indicate the MSE obtained using the mesh minimizing MSE on the reference sample.

**Experimental setup.** We train for 50,000 steps using a batch size of 32. An initial learning rate of  $10^{-3}$  is used with an exponential decay factor of 0.98 applied every 1000 steps. At every step, we randomly sample 30% of the points to be fed to the encoder. The decoder and loss are evaluated on the complement (i.e., 70%) of these points. We have found that this ratio provides a good balance of robustness to different masks and overall performance.

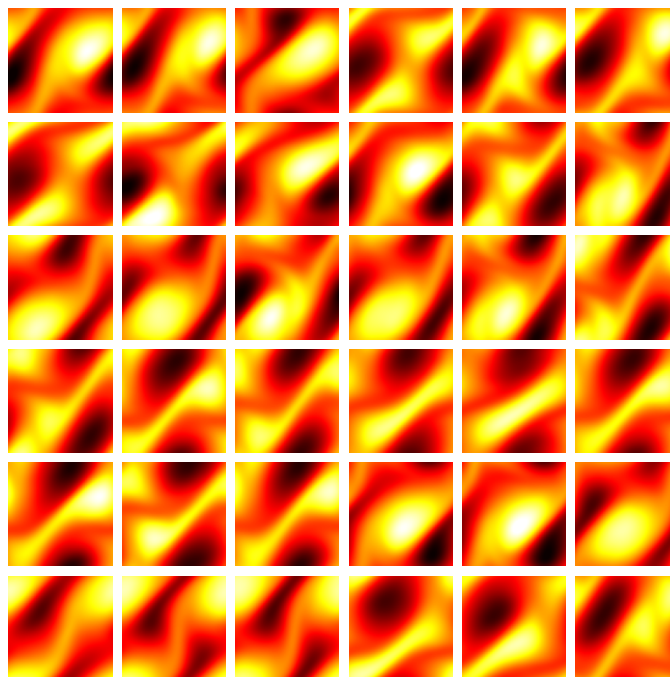
**Architecture.** For the sake of comparison, we define a standard CNN-based FAE following the VGG-inspired methodology (Simonyan and Zisserman, 2015) of gradually contracting/expanding the feature map while increasing/decreasing the channel dimensions. The architecture is adapted to have a similar parameter count to our baseline FAE model. Both of these models use Gaussian random positional encodings with  $k = 16$ .

The encoder consists of four CNN layers with output channel dimension 4, 4, 8, and 16 respectively and kernel sizes are 2, 2, 4, and 4 respectively, all with stride 2. The result is flattened and passed through a single-hidden-layer MLP of width 64 to obtain a vector of dimension 64. The decoder consists of a single-layer MLP of width 64 and output dimension 512, which is then rearranged to a  $4 \times 4$  feature map with channel size 32. This feature map is then passed through four layers of transposed convolutions that respectively map to 16, 8, 4, and 4 channel dimensions, with kernel sizes 4, 4, 2, and 2 respectively, and stride 2. The result is then mapped by two CNN layers with kernel size 3, stride 1, and output channel dimension 8 and 1 respectively.

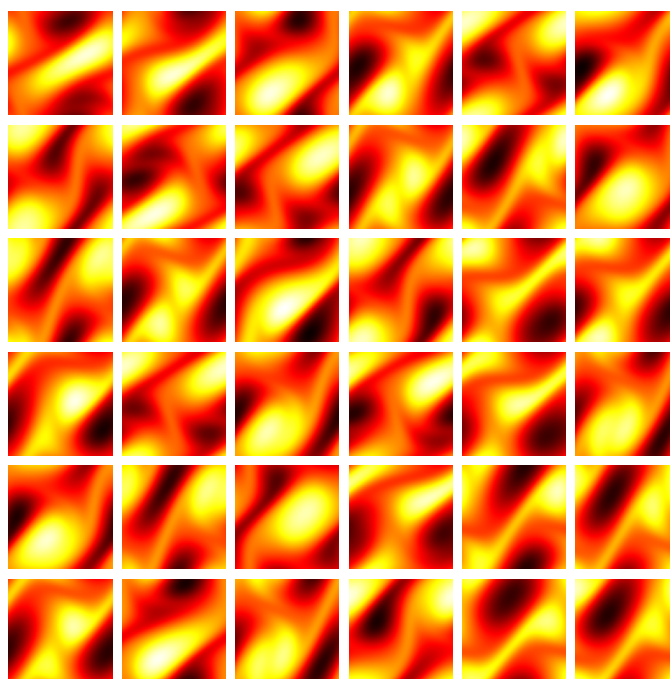
**Uncurated samples.** As described in Section 4.3.2, we apply FAE as a generative model by fitting a Gaussian mixture with 10 components on the latent space. Samples from the generative model trained at at viscosity  $\nu = 10^{-3}$ ,  $\nu = 10^{-4}$  and  $\nu = 10^{-5}$  are provided in Figures B.7, B.8, and B.9 respectively.

**Uncurated reconstructions.** Reconstructions from randomly selected data from the held-out sets for viscosities  $\nu = 10^{-3}$ ,  $\nu = 10^{-4}$  and  $\nu = 10^{-5}$  are provided in Figures B.10, B.11, and B.12 respectively.

**Evaluation at very high resolutions.** In Figure 4.4, we demonstrate zero-shot resolution by evaluating the decoder on grids of resolution  $2,048 \times 2,048$  and  $32,768 \times 32,768$ . We point out that, while the former requires approximately 16 MB to store using 32-bit floating point numbers, the latter requires 4.3 GB, vastly exceeding the available memory of typical consumer GPUs. To allow evaluation of the decoder at this resolution, we partition the domain into 1,000 chunks and evaluate the decoder on each chunk in turn and reassemble the resulting data in the RAM. To ensure that each chunk has an integer number of points, we take the first 824 chunks to contain 1,073,742 mesh points (approximately 4 MB), and take the remaining 176 chunks to contain 1,073,741 points.

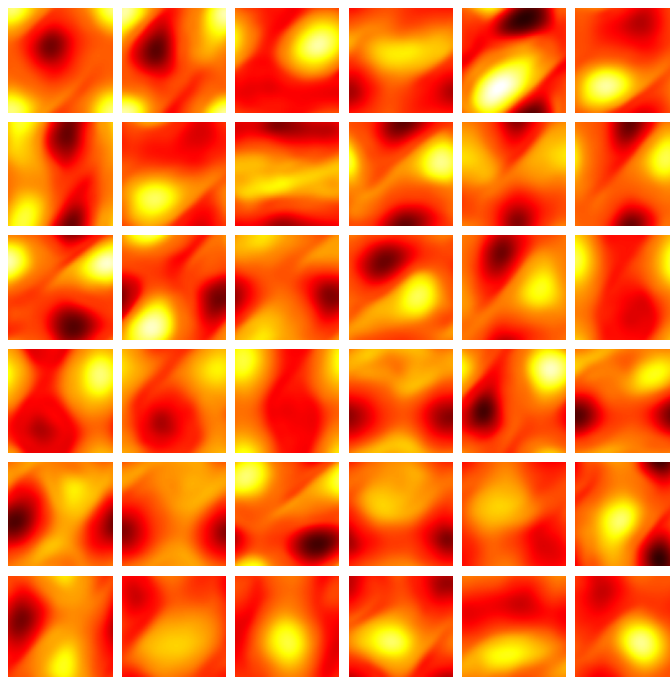


(a) FAE

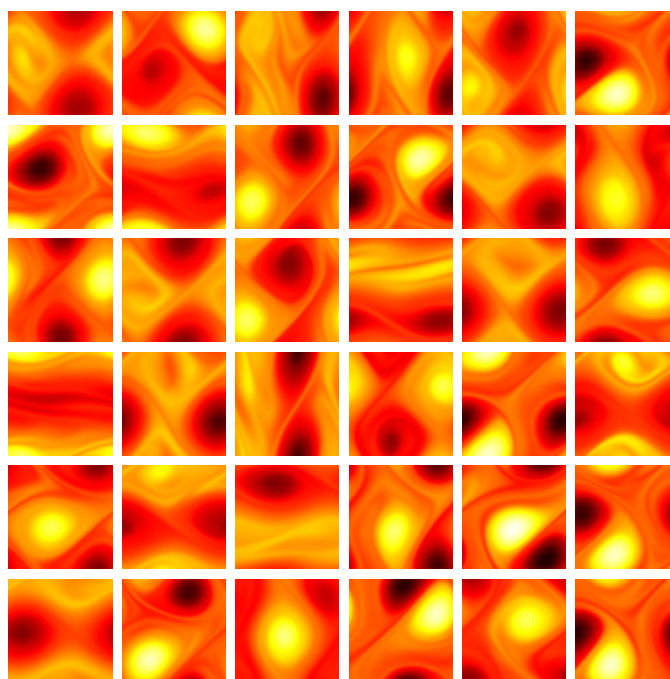


(b) Dataset

Figure B.7: Samples of Navier–Stokes data with viscosity  $\nu = 10^{-3}$ .



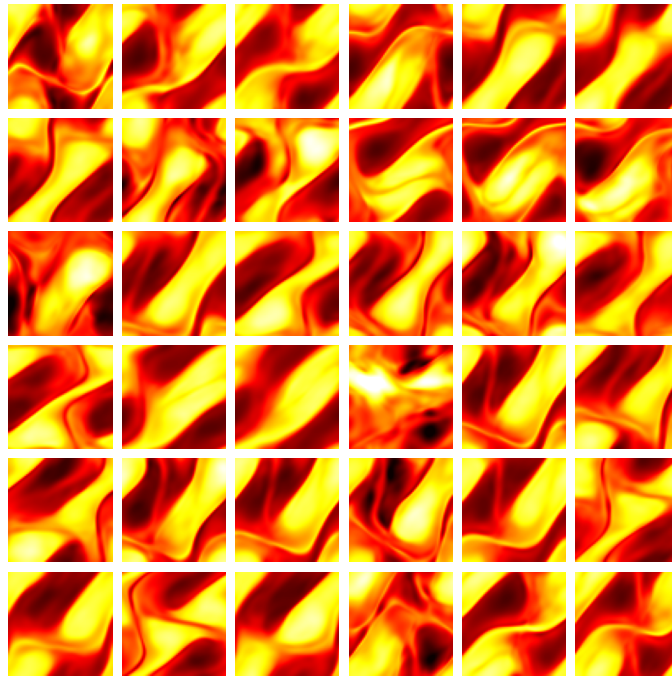
(a) FAE



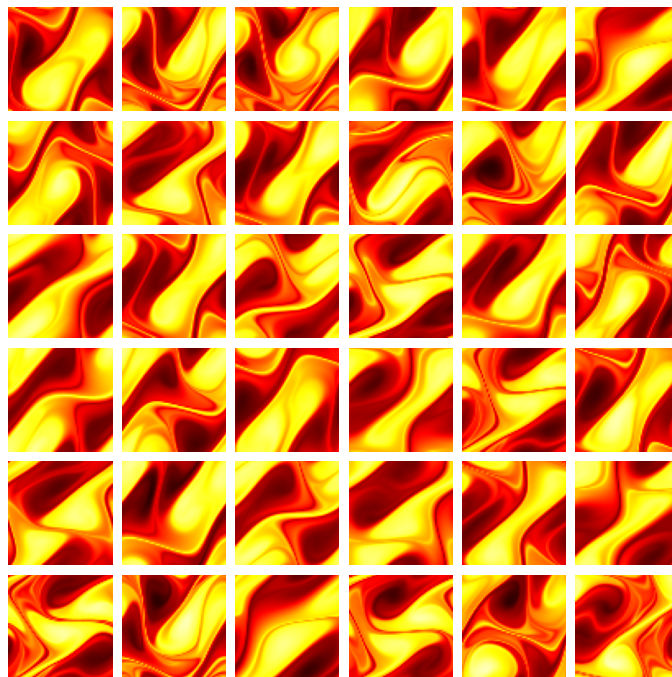
(b) Dataset

Figure B.8: Samples of Navier–Stokes data with viscosity  $\nu = 10^{-4}$ .





(a) FAE



(b) Dataset

Figure B.9: Samples of Navier–Stokes data with viscosity  $\nu = 10^{-5}$ .



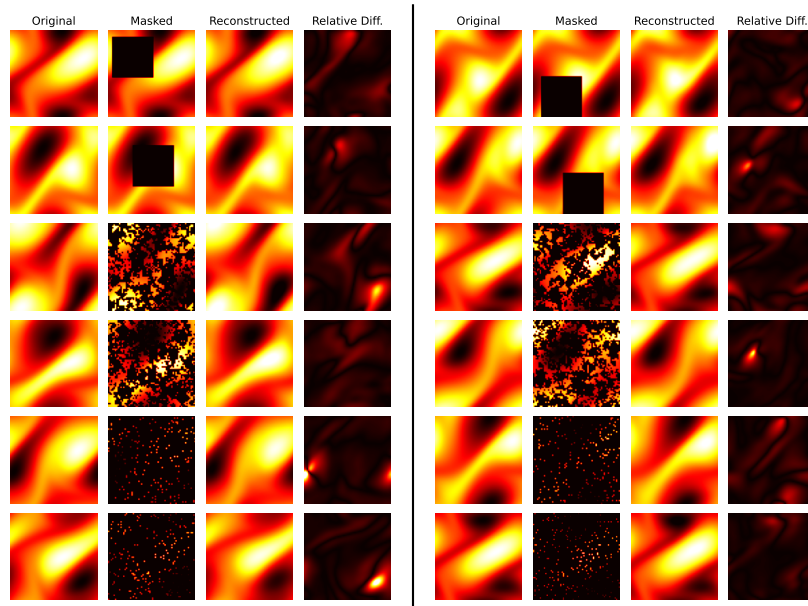


Figure B.10: FAE reconstructions of Navier–Stokes data with viscosity  $10^{-3}$ .

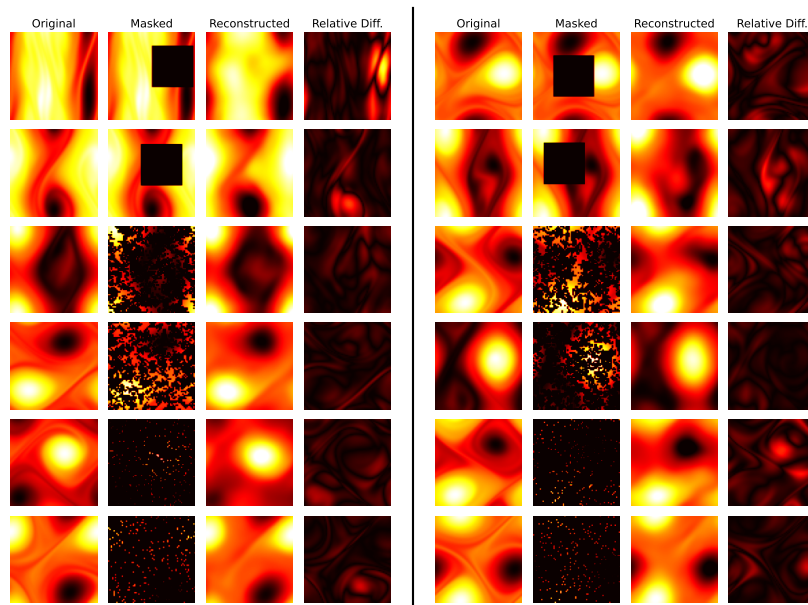


Figure B.11: FAE reconstructions of Navier–Stokes data with viscosity  $10^{-4}$ .

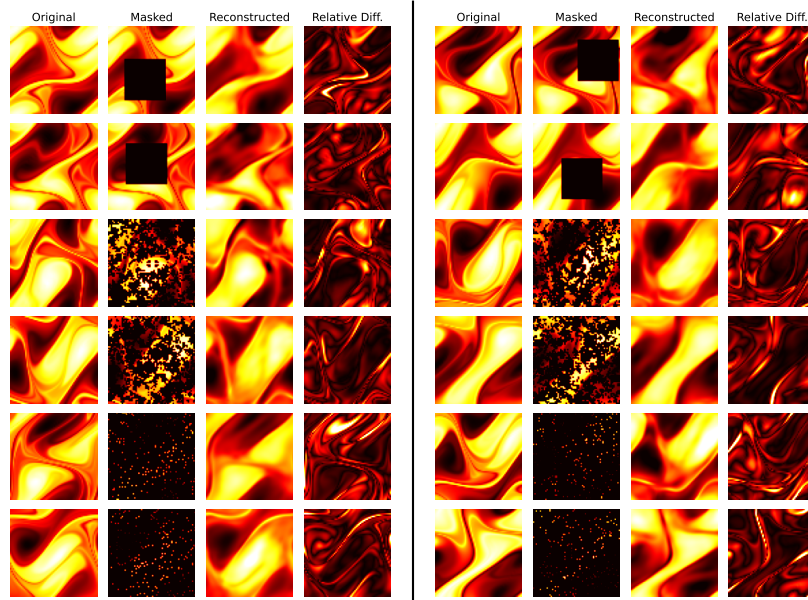


Figure B.12: FAE reconstructions of Navier–Stokes data with viscosity  $\nu = 10^{-5}$ .

### B.6 Darcy Flow

**Data and discretisation.** The dataset used in Section 4.3.2 is based on that of Li et al. (2021), provided on a  $421 \times 421$  grid and generated through a finite-difference scheme. Where described, we downsample this data to lower resolutions by applying a low-pass filter in Fourier space and subsampling the resulting filtered image. The low-pass filter is a mollification of an ideal sinc filter with bandwidth selected to eliminate frequencies beyond the Nyquist frequency of the target resolution, computed in practice by convolving the ideal filter in Fourier space with a Gaussian kernel of with standard deviation  $\sigma = 0.1$ , truncated to a  $7 \times 7$  convolutional filter.

**Experimental setup.** We follow the same setup used for the Navier–Stokes dataset: we train for 50,000 steps, with batch size 32 and random sampling of 30% of points in the encoder, evaluating the decoder on the unseen mesh points. An initial learning rate of  $10^{-3}$  is used with an exponential decay factor of 0.98 applied every 1000 steps. We also make use of positional embeddings (Appendix B.1) using  $k = 16$  Gaussian random Fourier features.

When performing the wall-clock training time experiment (Figure 4.6(a)), we downsample the training and evaluation data to resolution  $211 \times 211$ . For the zero-shot superresolution experiment (Figure 4.6(b)), we downsample training data, and the encoder inputs during evaluation, to resolution  $53 \times 53$ . For the FAE generative model experiment, we downsample training and evaluation data to resolution  $47 \times 47$ .

**Uncurated reconstructions.** Reconstructions of randomly selected examples from the held-out evaluation dataset are shown in Figure B.13.

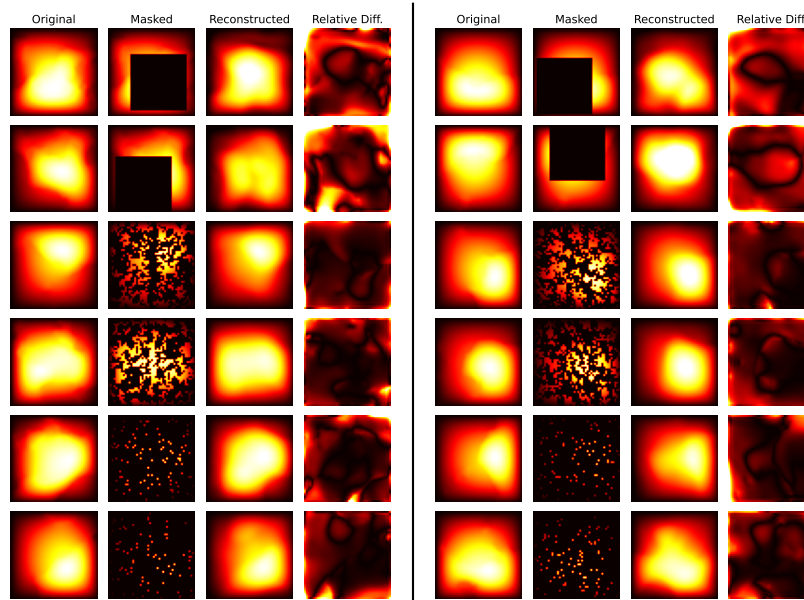
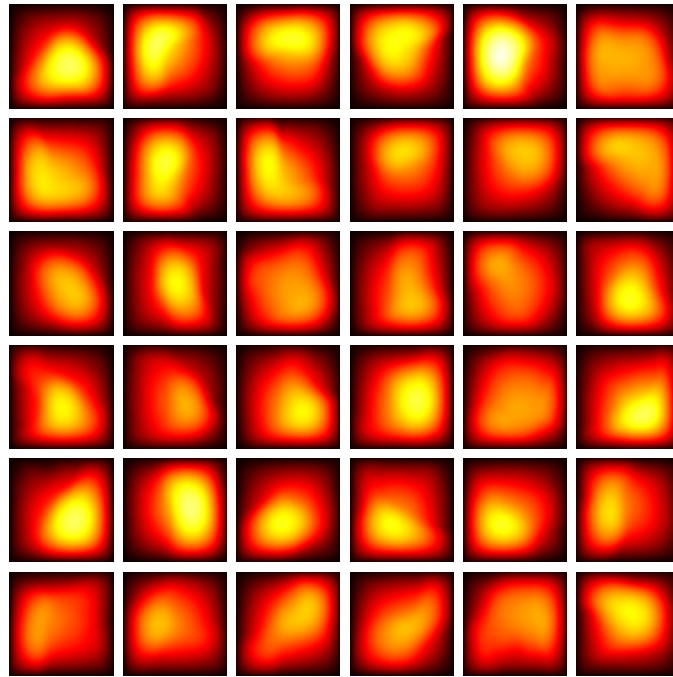
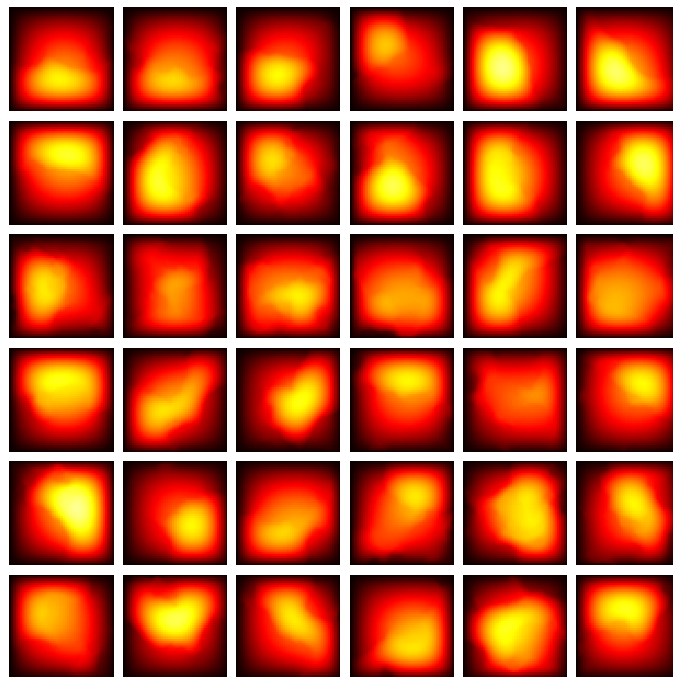


Figure B.13: FAE reconstructions of Darcy flow data.

**Uncurated samples.** Samples from the FAE latent generative model and random draws from the evaluation dataset are shown in Figure B.14.



(a) FAE



(b) Dataset

Figure B.14: Samples of Darcy flow data.